Fast generation of spectrally shaped disorder

Aaron Shih [1,2,*] Mathias Casiulis [2,3,*] and Stefano Martiniani [1,2,3,†]

[1] *Courant Institute of Mathematical Sciences, New York University, New York 10003, USA*
[2] *Center for Soft Matter Research, Department of Physics, New York University, New York 10003, USA*
[3] *Simons Center for Computational Physical Chemistry, Department of Chemistry, New York University, New York 10003, USA*

Media with correlated disorder display unexpected transport properties, but it is still a challenge to design structures with desired spectral features at scale. In this work, we introduce an optimal formulation of this inverse problem by means of the nonuniform fast Fourier transform, thus arriving at an algorithm capable of generating systems with arbitrary spectral properties, with a computational cost that scales $\mathcal{O}(N \log N)$ with system size. The method is extended to accommodate arbitrary real-space interactions, such as short-range repulsion, to simultaneously control short- and long-range correlations. We thus generate the largest-ever stealthy hyperuniform configurations in $2d$ ($N = 10^9$) and $3d$ ($N > 10^7$) and demonstrate the flexibility of the approach by generating structures with designed spectral features at scale. By an Ewald sphere construction we link the spectral and optical properties at the single-scattering level and show that stealthy hyperuniform structures generically display transmission gaps, providing a concrete example of fine-tuning of a physical property. We also show that large $3d$ power-law hyperuniformity in particle packings leads to single-scattering properties nearly identical to those of simple hard spheres. Finally, we demonstrate generalizations of the approach to impose features in either continuous or discrete real space, using constraints in either continuous or discrete reciprocal space. In particular, enforcing large spectral power at peaks with the right symmetry leads to the nondeterministic generation of quasicrystalline structures in $2d$ and $3d$. This technique should become an essential tool to embed, and understand the role of, long-range correlations in disordered metamaterials.

I. INTRODUCTION

The study of condensed matter is often facilitated by the periodicity of atomic structures. For instance, photonic band gaps in crystals can be predicted by Bloch's theorem [1]. In contrast, analytic models are still being developed to understand the emergent optical properties of *disordered media* [2,3], i.e., materials that do not exhibit conventional forms of long-range order. Among disordered materials, systems with *correlated disorder*, whose structures are non-Poissonian random point patterns, have garnered attention following experimental and computational reports of unconventional scattering properties: structural coloration [4,5], isotropic band gaps [6,7], or Anderson localization [8,9].

Beyond condensed matter, correlated point patterns are crucial to computer graphics [10,11], and various protocols have been introduced to impose prescribed spatial correlations between points [10–12]. These strategies amount to an optimal sampling problem: Given some natural image, where should a finite number of sample points be placed in order to minimize aliasing errors? A common answer is to use *blue-noise sampling* [10], i.e., point patterns with highly suppressed long-ranged pair correlations but no clear periodicity. In. practice, the best such point patterns have strictly zero low-frequency content [12].

Physicists refer to such point patterns as *disordered hyperuniform* structures [13]. It has been argued that these structures exhibit photonic band gaps and localization due to their suppressed long-range density fluctuations [6–9,14,15]. To produce hyperuniform point patterns with prescribed correlated disorders, the best-known algorithm relies on the collective coordinate approach [16,17], which minimizes differences between an observed structure factor and a desired one using gradient optimization. These algorithms suffer from a major drawback: Their algorithmic complexity is $\mathcal{O}(N^2)$ [18] or even $\mathcal{O}(N^3)$ [16,17] in the number, N, of points. Consequently, the vast majority of hyperuniform systems studied in the literature contain modest numbers of points (10^2 to 10^4 points [16,17,19], more recently up to $\sim 10^6$ points using a massively parallel GPU implementation [18]), and were overwhelmingly limited to one specific kind of hyperuniformity to make calculations tractable [9,18,20]. These limitations have also critically affected the scale of additively manufactured hyperuniform materials, typically a few hundreds of particles only [6,7,21], which is particularly problematic in $3d$ [15,22] as the linear size of the system reaches only tens of particles across. This raises the question of whether the structures used in past studies truly encoded hyperuniformity, an inherently long-range property.

In this paper, we introduce a powerful optimization algorithm, sketched in Fig. 1(a), that can generate spectrally shaped disordered point structures with arbitrary spectral features [see Figs. 1(b)–1(e)]. In short, the algorithm resorts to nonuniform fast Fourier transforms (nuFFTs) to efficiently

---

*These authors contributed equally to this work
†Contact author: sm7683@nyu.edu
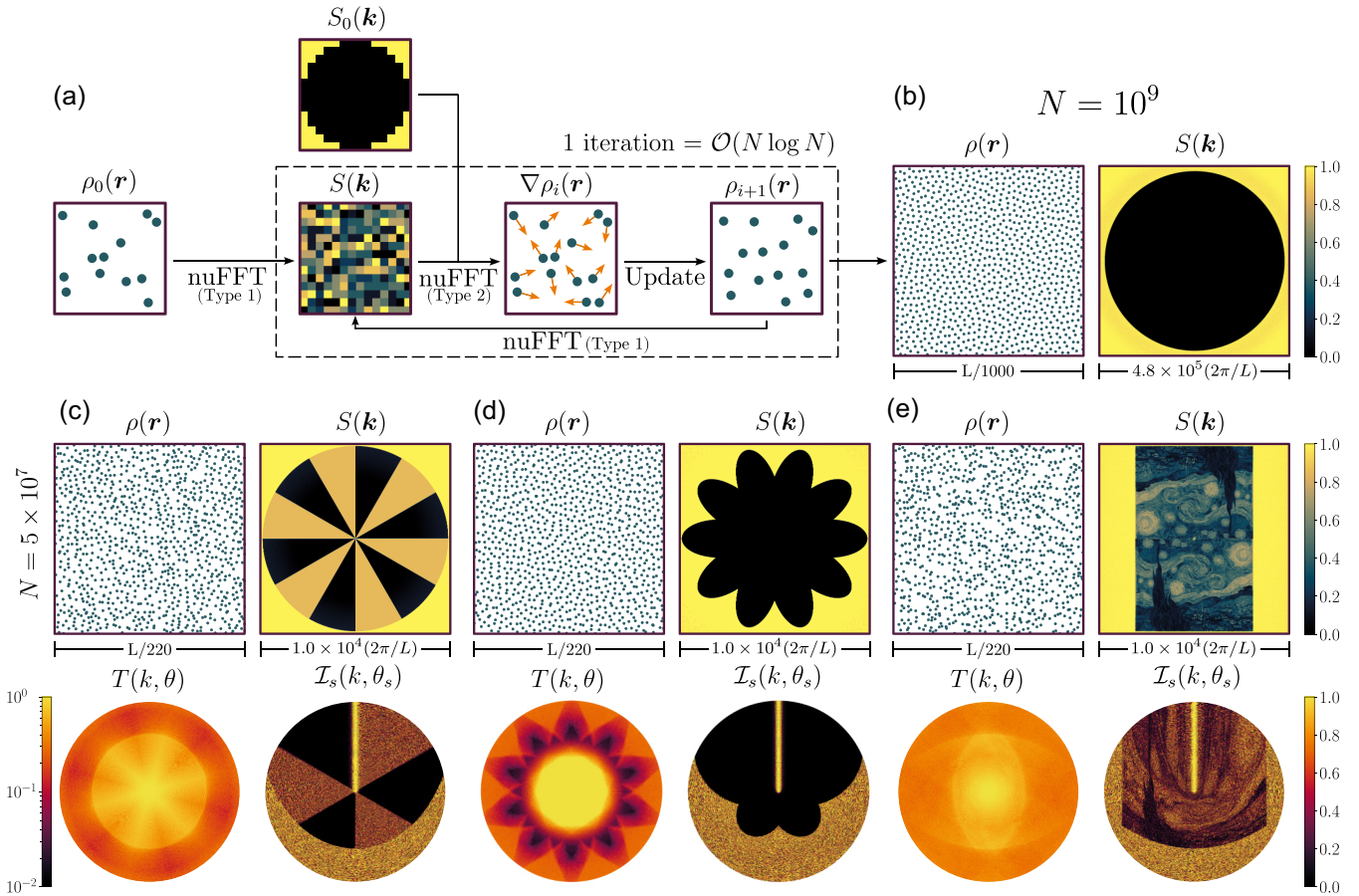
FIG. 1. Fast reciprocal-space correlator (FReSCo): (a) Sketch of the implementation of our algorithm. A point pattern $\rho_0(\boldsymbol{r})$ is subjected to a nuFFT transformation, so that a loss can be computed from the difference between the observed k-space structure, $S(\boldsymbol{k})$, and a target function, $S_0(\boldsymbol{k})$. The gradient of this loss is obtained as another nuFFT, so that each iteration of the optimization can be performed in $\mathcal{O}(N \log N)$ operations. (b) Example output of the algorithm: We show a small portion of an $N = 10^9$ point pattern, as well as the final structure factor. [(c)–(e)] A few example outputs imposing a variety of target structures to smaller systems ($N = 5 \times 10^7$ points): From left to right, a pinwheel, a 10-petaled flower structure factor, and the lightness scale of Van Gogh's *The Starry Night* [23]. In each panel, we show a portion of the final point pattern (top left), structure factor (top right), forward scattering transmission, $T(k, \theta)$, as a function of the magnitude, k, and orientation, θ, of an incoming wave (bottom left), and scattered intensity, $\mathcal{I}_s(k, \theta_s)$ (bottom right) for an upward incident wave vector, as a function of the incident frequency, k, and of the scattered direction, θ_s.

compute the structure factor $S(\boldsymbol{k})$ of a point pattern $\rho(\boldsymbol{r})$. The distance from $S(\boldsymbol{k})$ to a prescribed target $S_0(\boldsymbol{k})$ then defines a loss function. Crucially, we show that the gradient of this loss can also be written as a nuFFT, so that the cost of one step in a minimization procedure scales quasilinearly in the system size, $\mathcal{O}(N \log N)$. This cost function can be jointly optimized with additional physical constraints, such as short-ranged pair repulsion, with no increase in computational complexity.

We demonstrate its application for as many as 10^9 points [Fig. 1(b)], outperforming (by at least three orders of magnitude) all previously published methods possessing the same specificity in k space for point patterns [16–18]. The target structure factor, S_0, can be chosen at will as long as the number of k-space features being constrained does not exceed the number of degrees of freedom. We show a few smaller ($N = 5 \times 10^7$) examples in Figs. 1(c)–1(e), where we embed a pinwheel (c), a 10-fold flower (d), or Van Gogh's *The Starry Night* (e) [23] into the structure factor. We also show [Figs. 1(c)–1(e)] that the optical

properties of such structures can be characterized in the single-scattering regime on the scale of realistic devices, without assuming periodicity. We show the forward-scattered transmission pattern, T, of these structures against the wave vector of an incoming plane wave, as well as the intensity, $\mathcal{I}_s$, of the scattered field in each direction, for an upward incident wave, across frequencies (see precise definitions below).

In the following, we highlight the range of applications of this algorithm. We show that unquestionably stealthy hyperuniform systems (i.e., with hyperuniform density fluctuations scalings spanning over three decades; see Appendix F) have transmission gaps even at the single-scattering level. However, we show that particle systems with power-law behavior in S (like particles at jamming [24] or critical absorbing-state models [25,26]) have single-scattering properties indistinguishable from equilibrium hard spheres. We finally discuss extensions of fast reciprocal-space correlator (FReSCo), e.g., one that produces quasicrystalline structures [27] from very few constraints.

II. ALGORITHM

Consider a set of N points at d-dimensional positions, $\boldsymbol{r}_1, \ldots, \boldsymbol{r}_N \in \mathbb{R}^d$, each carrying a weight $c_n \in \mathbb{C}$. One may define a density field as the sum of N Dirac deltas, $\rho(\boldsymbol{r}) \equiv \sum_n c_n \delta(\boldsymbol{r} - \boldsymbol{r}_n)$. In Fourier space, $\widehat{\rho}(\boldsymbol{k}) = \sum_n c_n \exp(i\boldsymbol{k} \cdot \boldsymbol{r}_n)$, so that one may define the structure factor,

$$S(\boldsymbol{k}) \equiv \frac{|\widehat{\rho}(\boldsymbol{k})|^2}{N}, \tag{1}$$

which encodes the two-point correlations of ρ [28]. FReSCo implements a minimization protocol against a loss, $\mathcal{L}_S$, defined as the least-squares error between $S(\boldsymbol{k})$ and a prescribed target, $S_0(\boldsymbol{k})$, in a finite region $\mathcal{K}$ of reciprocal space:

$$\mathcal{L}_S[(\boldsymbol{r}_1, c_1), \ldots, (\boldsymbol{r}_N, c_N)] = \sum_{\boldsymbol{k} \in \mathcal{K}} w(\boldsymbol{k}) L[S(\boldsymbol{k}), S_0(\boldsymbol{k})], \tag{2}$$

where $w(\boldsymbol{k})$ is a weighting function, and

$$L[S(\boldsymbol{k}), S_0(\boldsymbol{k})] = \begin{cases} [(S(\boldsymbol{k}) - S_0(\boldsymbol{k}))/S_0(\boldsymbol{k})]^2 & \text{if } S_0(\boldsymbol{k}) \neq 0 \\ S(\boldsymbol{k})^2 & \text{otherwise} \end{cases} \tag{3}$$

penalizes the relative distance to $S_0(k)$. We choose $w(\boldsymbol{k}) \sim |\boldsymbol{k}|^{-(d-1)}$ when $S_0(\boldsymbol{k})$ has pronounced radial symmetry around $k = 0$, so that k-space constraints are equally strong on every spherical shell. For instance, this applies to the structure factors of Figs. 1(b)–1(d), while for panel (e) we choose $w(\boldsymbol{k}) = 1$ (parameters for the runs are given in Appendix A).

Gradients of this loss can be written both with respect to weights and positions, with either periodic or free boundary conditions (see Appendix B). We first focus on the optimization of continuous positions with periodic boundary conditions and $c_n = 1$, a problem formally equivalent to that introduced in the collective coordinate approach [16–18]. In that case, $\rho(\boldsymbol{r})$ is real valued and $S(\boldsymbol{k}) = S(-\boldsymbol{k})$, a property known in crystallography as Friedel's law [29], so that only centrosymmetric S are realizable. For instance, embedding *The Starry Night* [23] in the $k_y < 0$ half-plane leads to its inversion being constrained for $k_y > 0$ in Fig. 1(e). Using Eq. (1), the gradients of the loss function can be written as Fourier transforms (see Appendix B),

$$\frac{\partial \mathcal{L}_S}{\partial \boldsymbol{r}_n} = \text{Re}\left[\sum_{\boldsymbol{k}} \boldsymbol{C}(\boldsymbol{k}) c_n \exp(-i\boldsymbol{k} \cdot \boldsymbol{r}_n) \right] = c_n \text{Re}[\widehat{\boldsymbol{C}}(\boldsymbol{r}_n)], \tag{4}$$

where $\boldsymbol{C}(\boldsymbol{k}) = -4i\boldsymbol{k} w(\boldsymbol{k})[S(\boldsymbol{k}) - S_0(\boldsymbol{k})]\widehat{\rho}(\boldsymbol{k})/N$ are coefficients of a Fourier series and $\widehat{\boldsymbol{C}}$ is the Fourier transform of $\boldsymbol{C}$.

This rewriting of the gradient constitutes the core idea behind FReSCo. Previous algorithms [16–18] explicitly computed the gradient of the loss as a double sum over particles, requiring $\mathcal{O}(N^2)$ operations per k, with a number of constraints scaling linearly in N, resulting in $\mathcal{O}(N^3)$ operations per gradient evaluation in a brute-force approach [16,17] or $\mathcal{O}(N^2)$ if the Fourier transform of the density field is precomputed [18]. In our approach, in total, one FFT is required to compute $\mathcal{L}_S$ and d additional FFTs are required for the gradient of $\mathcal{L}_S$. We therefore bypass the double sum and bring down the number of operations to that of a single FFT, $\mathcal{O}(N \log N)$, for both loss and gradient calls. As these are the most costly

steps in calculating the loss, they dominate the cost of the whole minimization, which also scales like $\mathcal{O}(N \log N)$ (see benchmarks in Appendix D), nearly N times faster per step than previous implementations, meaning that a full minimization is many orders of magnitude faster at the values of N we explore. To compute FFTs, we rely on the Flatiron Institute nonuniform fast Fourier transform (FINUFFT) implementation of nonuniform fast Fourier transforms [30,31]. With the state-of-the-art optimizations built into FINUFFT, the computational speed increase is enormous, enabling the generation of correlated disordered systems up to $N = 10^9$ on CPUs [Fig. 1(b)], the main limitation being memory requirements. The optimization is performed by feeding the configuration and gradient to L-BFGS [32], a quasi-Newton method, with a maximal step size and a backtracking line search [33]. An efficient and easy-to-use. implementation of FReSCo is publicly available [34].

III. STRUCTURE AND SCATTERING

To characterize the optical behavior of systems at scale without introducing artificial periodicity, we proceed as follows. First, like in experiments [7], we cut the optimized point patterns into disks to avoid anisotropy coming from the shape of the medium; then we use the Ewald sphere construction [1] on the resulting object by means of FINUFFT transformations [see sketch in Fig. 2(a)]. We remind that the Ewald sphere construction is equivalent to the far-field single-scattering response in the Supplemental Material (SM) [35] and illustrate the technique in Fig. 2(b). In short, at single-scattering level, for an incident wave vector $\boldsymbol{k}_{\text{inc}}$, the far-field intensity scattered with wave vector $\boldsymbol{k}_{\text{sca}}$ is proportional to $S(\boldsymbol{q})$ at $\boldsymbol{q} = \boldsymbol{k}_{\text{sca}} - \boldsymbol{k}_{\text{inc}}$ [2]. Therefore, we read off the single-scattering response at any given frequency, and in any observation direction, by drawing a sphere centered at $-\boldsymbol{k}_{\text{inc}}$ with radius $k = |\boldsymbol{k}_{\text{inc}}| = |\boldsymbol{k}_{\text{sca}}|$. In Fig. 2(b), we illustrate this procedure and show the scattered intensity profile, $\mathcal{I}_s$, for a single incident illumination direction against the wave-vector magnitude k (radial direction) and the observation direction θ_s (orthoradial direction). In order to account for a finite detection width, we also define a normalized $2d$ transmission,

$$T(\boldsymbol{k}_{\text{inc}}) = \frac{\int_{\mathcal{F}\backslash 0} S[k\hat{\boldsymbol{e}}(\theta + \vartheta) - k\hat{\boldsymbol{e}}(\theta)] d\vartheta}{\oint_{\mathcal{C}\backslash 0} S[k\hat{\boldsymbol{e}}(\theta + \vartheta) - k\hat{\boldsymbol{e}}(\theta)] d\vartheta}, \tag{5}$$

where the angle ϑ between the incident and scattered waves is integrated over the forward half-circle $\mathcal{F} \subset \mathcal{C}$ around the incident direction θ, and the normalization is the total scattered intensity on the full circle, $\mathcal{C}$, removing from both integrals the direction $\vartheta = 0$ [that reduces to the peak $S(\boldsymbol{0}) = N$]. We extend this definition to $3d$ by replacing ϑ by a solid angle and the (half-)circle by a (half-)sphere.

In Fig. 2(c), we show one example of the possibilities offered by FReSCo: a spiral-shaped domain of zeros in the structure factor of $N = 5 \times 10^7$ particles leads to fringes of low scattered intensities in a range of frequencies and to a spiral-shaped transmission pattern. This example and those of Fig. 1(c) demonstrate that achieving fine control over $S(\boldsymbol{q})$ in large point patterns enables the design of intricate scattering behaviors.
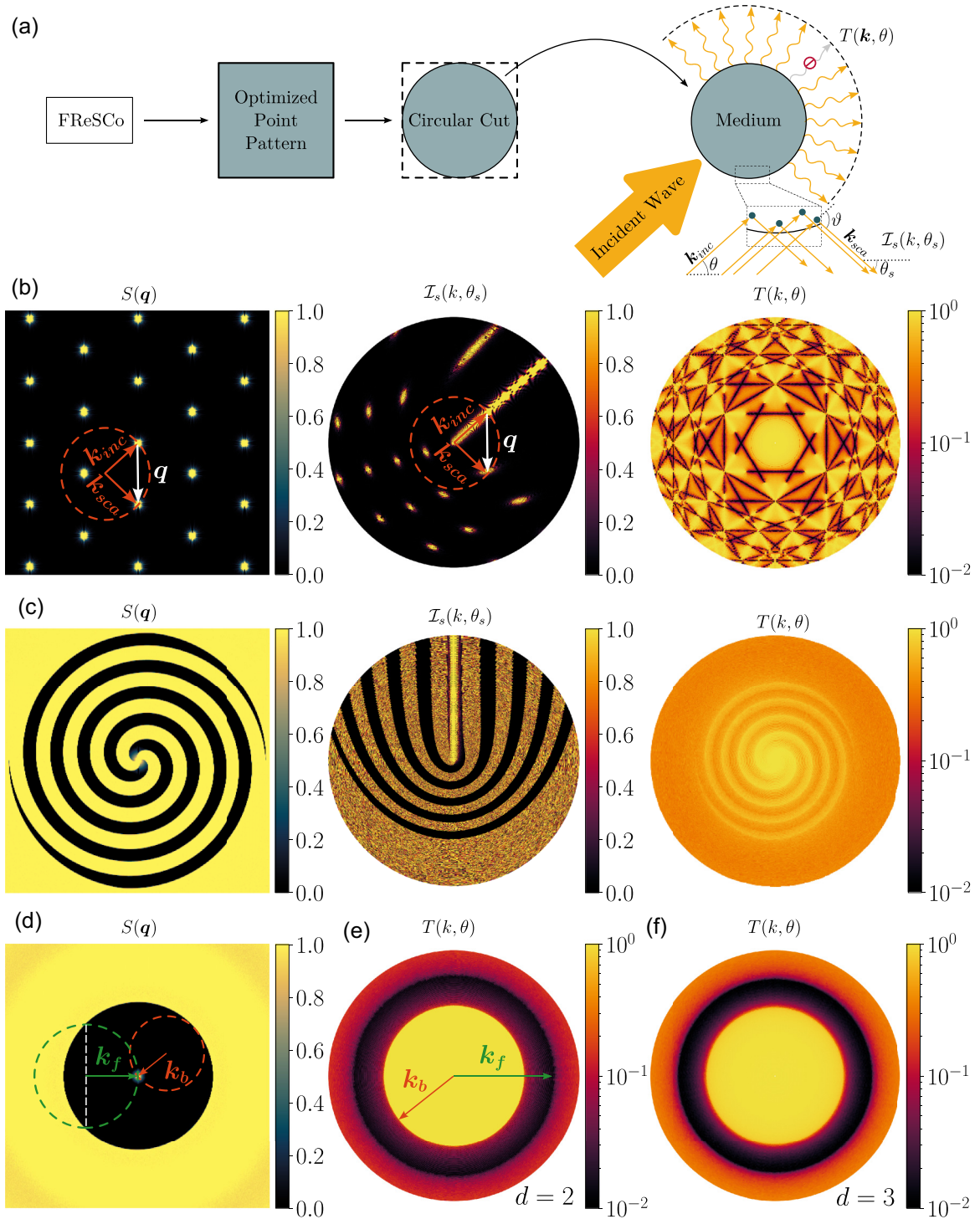
FIG. 2. Ewald sphere construction and single scattering. (a) Sketch of single-scattering analysis. From an optimized structure, we cut the central disk and then measure its single-scattering properties. To an incoming wave vector, k_{inc}, we associate the far-field, normalized scattered intensity, $\mathcal{I}_s$, in direction θ_s. (b) Illustration of the Ewald circle construction on a $2d$ triangular lattice. From the structure factor $S(q)$ (left) evaluated at $q = k_{sca} - k_{inc}$, we obtain $\mathcal{I}_s$ (middle) which, once integrated, yields the transmission, T, as a function of the incident wave vector (right). (c) Example of an optimized $2d$ point pattern ($N = 5 \times 10^7$) with a spiral of zeros in its $S(q)$. (d) Structure factor, $S(q)$, and [(e) and (f)] transmission, T, results for generated stealthy hyperuniform structures, for (e) $N = 5 \times 10^7$ in $2d$ and (f) $N = 5 \times 10^6$ in $3d$ (right). In (d)–(e), we indicate the values k_b (shorter red arrow) and k_f (longer green arrow) above which back- and forward-scattering develop, respectively, based on the Ewald construction. In (c) and (e), $K = 5050$ and plots are shown up to $k_{max} = 4500$. In (f), $K = 142$, $k_{max} = 130$, and θ sweeps one arbitrary circle.

We take advantage of this approach to study stealthy hyperuniform structures, systems with $S(k) = 0$ in a disk of radius K, at scale. In Fig. 2(d) we show a typical structure factor and, in Figs. 2(e)–2(f), transmission plots, $T(k, \theta)$. On $S(\boldsymbol{q})$, we highlight two special values of k. The first such value, $k_b = K/2$, separates the domain $k < k_b$ in which the system is transparent (up to multiple scattering effects [20,22]) from the domain $k > k_b$ in which the system backscatters, as the back of the Ewald circle overlaps with high values of $S(\boldsymbol{q})$. The second special value, $k_f = K/\sqrt{2}$, separates the regimes $k_b < k < k_f$, where only backscattering happens, and $k > k_f$, where forward-scattering sets in, down to narrower and narrower angles as the frequency increases. Therefore, one expects a trough of lower forward-scattered transmission at intermediate $k_b < k < k_f$, suggestive of an isotropic band gap, in a stealthy hyperuniform configuration. This picture is confirmed in the transmission plot of Fig. 2(e), obtained for a $2d$ configuration with $N = 5 \times 10^7$ points, where we report these values, and in Fig. 2(f), obtained for a $3d$ configuration with $N = 5 \times 10^6$ points.

This result constitutes the largest-scale direct check that stealthy hyperuniform systems do feature isotropic transmission gaps in $2d$ and $3d$, as well as the largest $3d$ hyperuniform systems altogether [15,36,37]. Note that a smaller angular integration domain in T (i.e., a smaller detector) leads to a broader transmission trough, $[k_b; k_f + \epsilon]$ with $\epsilon \geqslant 0$. By integrating over the full half-disk or half-sphere we are thus reporting the *narrowest* observable transmission gap; see Appendix G. Interestingly, numerical evidence of band gaps as well as experimental and numerical reports of transmission gaps were made for $2d$ stealthy hyperuniform systems [6–9,14,18,19]. However, to the best of our knowledge, no past work has clearly discussed that even at the level of single scattering—which *cannot* support a band gap (a low value of the density of optical states in the bulk of the system [8,9])—stealthy hyperuniform structures should exhibit an isotropic trough of lower transmission for a range of k. Since the vast majority of experimental studies on these systems have relied on small sample sizes, often using low index contrasts [6,7] and small detection angles, it may very well be that the reported low transmissions did not even require an actual band gap.

Furthermore, numerical reports of band gaps in these systems have often (with some notable exceptions [8,9]) relied on frequency-domain finite-difference band predictions for small periodicized systems [6,7,14], so that it is not clear whether these estimates truly captured the consequences of hyperuniformity (a long-range property).

In future work we will conduct a systematic study of large-scale structures designed by FReSCo, in particular hyperuniform ones, at the multiple scattering level to clearly establish the origin of low transmission in correlated disordered systems.

IV. DISORDERED HYPERUNIFORM STRUCTURES

A. Point patterns

We now focus on the quality of our disordered hyperuniform structures. From a k-space perspective, hyperuniformity
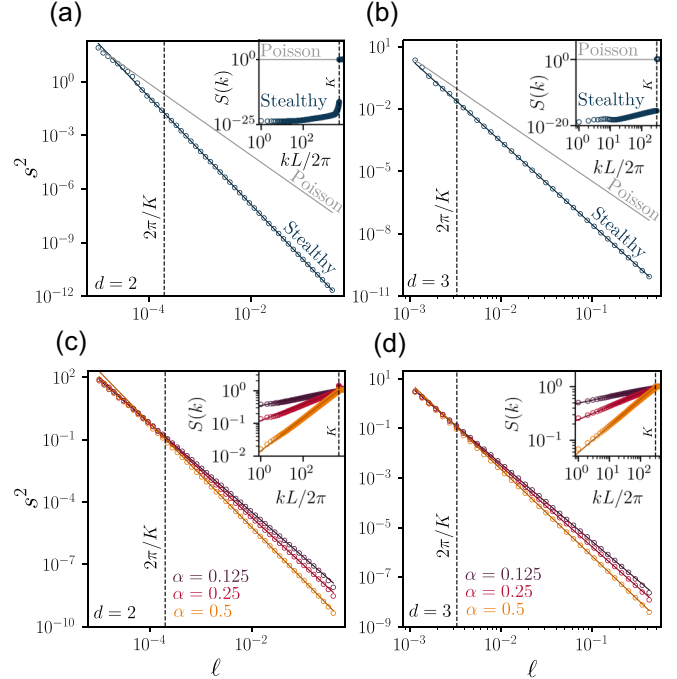
FIG. 3. Hyperuniform point patterns. [(a) and (b)] Number fluctuations against measurement window size (main panel) and structure factor (inset) for stealthy hyperuniform systems. We indicate the stealthy $\ell^{-(d+1)}$ (dark blue) and Poisson ℓ^{-d} (gray) scalings as solid lines, as well as a Poisson structure factor $S(k) = 1$ in the inset. [(c) and (d)] Same plots for power-law hyperuniform structures with exponents $\alpha \in \{0.125, 0.25, 0.5\}$ in (c) $2d$ and (d) $3d$. We show next to each curve the expected power law, $\ell^{-(d+\alpha)}$, in the main panels, and $S(k) \sim k^\alpha$ in the insets, with solid lines. Across (a)–(d), we show the radius K of the constrained disk in Fourier space, and the corresponding length scale $\ell = 2\pi/K$, as dashed lines. In all panels, $N = 5 \times 10^7$.

is associated with an anomalous decay of the structure factor, $S(\boldsymbol{k})$, at long range, or $S(\boldsymbol{k}) \to 0$ when $|\boldsymbol{k}| \to 0$. How the structure factor decays depends on the class of hyperuniform system [13]. We investigate two types of disordered hyperuniformity: stealthy and power law. Stealthy hyperuniformity occurs when $S(\boldsymbol{k}) = 0$ for $|\boldsymbol{k}| < K$, like the examples of Figs. 1(b) and 2(d), while power-law hyperuniformity implies $S(\boldsymbol{k}) \sim |\boldsymbol{k}|^\alpha$ for $|\boldsymbol{k}| < K$ and $\alpha > 0$.

While the structure factors of the hyperuniform point patterns considered in the literature appeared consistent with a power law for a few k vectors [17,36], it is not obvious that density fluctuations were actually suppressed at long range, due to their limited sizes, particularly in $3d$. Concretely, hyperuniformity is achieved only if the variance in the number of points sampled across spheres grows *slower* than their volume, $s^2 \equiv \langle N^2 \rangle / \langle N \rangle^2 - 1 \sim \ell^{-\beta}$, with $d \leqslant \beta \leqslant d + 1$, while in an uncorrelated point pattern $s^2 \sim \ell^{-d}$. In the following, we show that FReSCo is able to generate structures for which these power laws are verified over several decades of ℓ. In Figs. 3(a) and 3(b), we show the radially averaged structure factors (insets) and the associated number fluctuations, shown as the reduced variance, s^2, against the radius of a measurement sphere (main panels) for $N = 5 \times 10^7$ in $2d$ and $3d$,

respectively. These disordered stealthy hyperuniform configurations are orders of magnitude larger than any previous realization [9,14–21], as well as the most solid evidence of stealthy hyperuniformity in a system being associated with a $s^2 \sim \ell^{-(d+1)}$ decay of number fluctuations.

Inspired by critical configurations of absorbing-phase models [25,26] and jammed packings [24], we also design power-law hyperuniform point patterns by constraining the structure factor $S(\boldsymbol{k}) \sim |\boldsymbol{k}|^\alpha$ such that the structure factor at the largest wave-vector magnitude being constrained is $S(K) = 1$. We minimize 10 configurations of $N = 5 \times 10^7$ point systems for power laws $\alpha \in \{0.125, 0.25, 0.5\}$. Figures 3(c) and 3(d) depict the final structure factors (insets) and the associated number fluctuations against ℓ (main panels) in $2d$ and $3d$, respectively. The decay in the variance matches the predicted trends, $s^2 \sim \ell^{-(d+\alpha)}$ [12,13], decades beyond the length scale $2\pi/K$. We stress that this is by far the largest, and most rigorous, test of the real-space properties of power-law hyperuniform point patterns reported to date.

B. Particle packings

Thus far, we only constrained Fourier-space properties of point patterns, so there was no notion of excluded volume: Two points could come arbitrarily close together. This generically precludes the fabrication of raw point patterns without the use of arbitrary geometric transformations [6]. In order to generate more physical systems, in line with previous works [38], we introduce a hybrid loss that combines the structure factor loss, Eq. (2), with a repulsive pair potential U_{rep},

$$\mathcal{L} = \mathcal{L}_S + \sum_{m < n} U_{\text{rep}}(\boldsymbol{r}_m - \boldsymbol{r}_n). \tag{6}$$

This variant of FReSCo is sketched in Fig. 4(a). As long as the potential is finite ranged, computing the loss or its gradient still takes $\mathcal{O}(N \log N)$ operations. One may also introduce polydispersity into the system by specifying individual particle diameters in U_{rep}, in which case, to get the correct definition of S for homogeneous polydisperse spheres, each particle should be weighed by the ratio of its d-dimensional volume, V_n, to the mean volume, $\langle V \rangle$, i.e., $c_n = V_n/\langle V \rangle$ in Eq. (4) [39]. Here we choose a monodisperse Hertzian potential, $U_{\text{rep}}(r) \propto (r - \sigma)^{2.5}$, with σ the repulsive diameter. We also adjust the prefactor of the power law and the extent, K, of the domain in which we constrain the structure factor such that the target, $S_0(K)$, smoothly interpolates the Percus-Yevick approximation for the structure factor of hard-sphere liquids in $3d$ [28] and a similar approximation in $2d$ [40]. Results thus obtained are shown in Fig. 4, in both $2d$ [Fig. 4(b)] and $3d$ [Fig. 4(c)]. Our results show that arbitrary long-range features can still be achieved in the presence of short-range constraints like excluded volume, which guarantees the fabricability of structures with actual physical objects.

We also generate the single-scattering Ewald transmissions of these $3d$ configurations. In Fig. 4(d) we show the resulting T_{HS} for an equilibrium hard-sphere configuration (obtained using event-chain Monte Carlo methods [41]) at $\phi = 0.25$ and, in Fig. 4(e), the relative change between T_{HS} and the transmission, T, of power-law hyperuniform structures [same as in Fig. 4(d)], radially averaged over incoming angles.
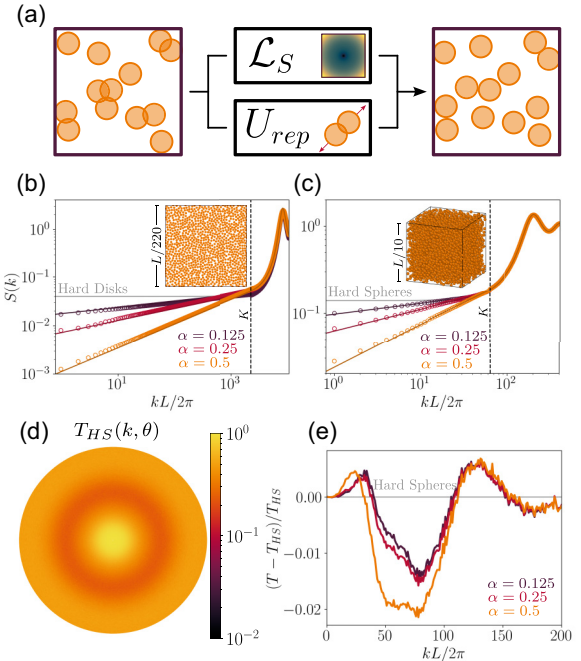
FIG. 4. Hyperuniform particle packings. (a) Sketch of the algorithm in the presence of both real- and reciprocal-space loss functions. From arbitrary initial conditions, we jointly optimize for prescribed features in k-space and short-range repulsion. [(b) and (c)] Structure factors of hyperuniform monodisperse (b) disk packings ($\phi = 0.6$) and (c) sphere packings ($\phi = 0.25$). Insets depict packings of the hyperuniform $\alpha = 0.5$ power-law systems. Structure factors are averaged over 10 realizations. (d) Forward-scattered transmission for equilibrium hard spheres at $\phi = 0.25$ up to $k_{\max} = 200$ and (e) relative change of forward-scattered transmission between $3d$ power-law hyperuniform structures of panel (c) and the starting equilibrium hard-sphere configuration. In (b), $N = 5 \times 10^7$, and $N = 4 \times 10^6$ in (c)–(e).

Power-law hyperuniformity, even in such large systems, does not significantly affect the scattering properties of hard-sphere systems in the single-scattering limit, as the largest relative change is only a few percentages. Thus hyperuniformity *per se*, as realized in critical systems like jammed packings, is not a necessary condition to observe a transmission gap in the single-scattering regime. This result is reminiscent of past work on stealthy hyperuniform structures [19].

V. FRESCO VARIANTS

So far, we only constrained nonuniform point positions with uniform k-space constraints (NUwU), but the same approach can be used with nonuniform k-space constraints (NUwNU). Furthermore, one may instead optimize the weights carried by uniform (on-grid) points, either with uniform (UwU) or nonuniform (UwNU) constraints in k space. These variants, whose gradients are derived in Appendix B, are illustrated with simple examples in Fig. 5. In UwU, while the real and Fourier spaces contain the same number of pixels [hence we are free to constrain the whole $S(\boldsymbol{k})$], we only constrain the modulus of a subset of k vectors, so that one may generate first guesses in phase retrieval problems [42],
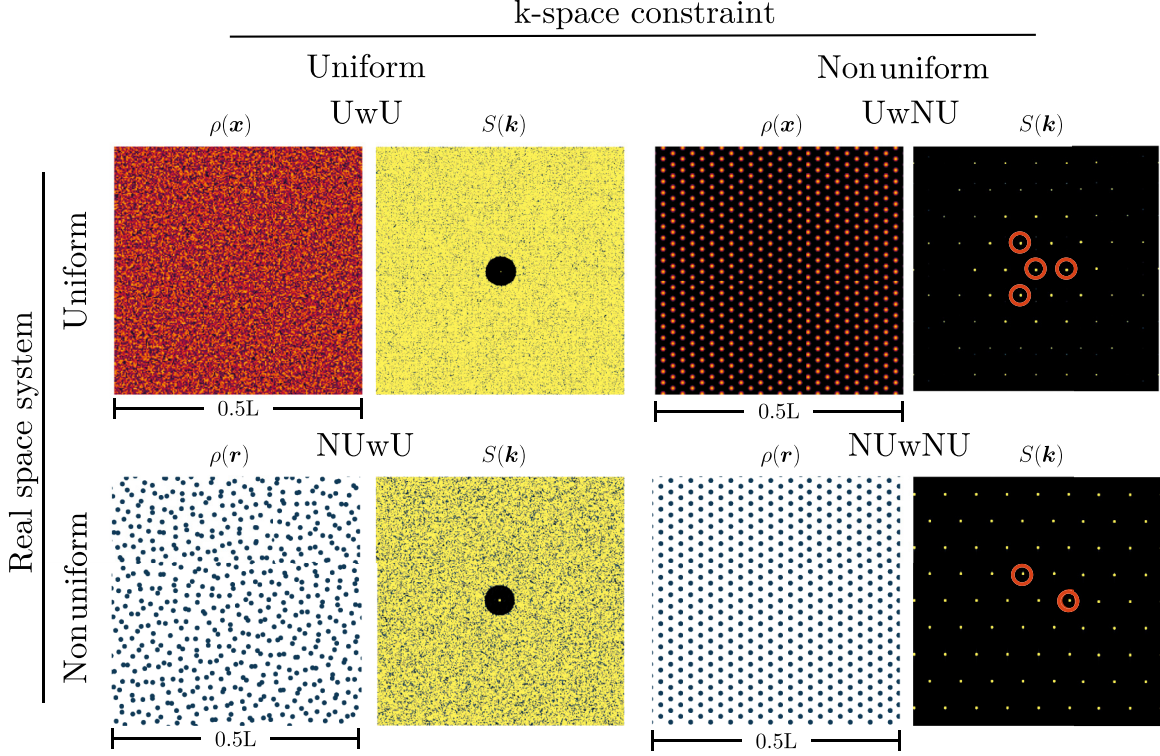
FIG. 5. Variations of FReSCo. We optimize the weights carried by a uniform (U) grid, or the positions of nonuniform (NU) sets of points in real space, while imposing constraints on a uniform grid or a nonuniform set of points in k space. Thus, we obtain four variants of the FReSCo algorithm: uniform real space with uniform k-space constraints (UwU), uniform real space with nonuniform k-space constraints (UwNU), nonuniform real space with uniform k-space constraints (NUwU), and nonuniform real space with nonuniform k-space constraints (NUwNU). Small example systems are provided (grid size 403×403 for uniform cases, $N \sim 2000$ points for nonuniform cases); see Appendix C for further analysis. In UwU and UwNU, we control the range of values of pixels via an external potential, and the total mass via a constraint on $S(k = 0)$, see Appendix B. Problems in which positions and weights are optimized simultaneously will be considered in future work.

textures with suitable properties [43], or random fields with suitable correlations [44]. In both UwNU and NUwNU, one may impose Fourier constraints at any continuous value, with free boundary conditions instead of periodic ones. In particular, we can impose constraints of the form $S_0 = \sum_p N\delta(\boldsymbol{k} - \boldsymbol{k}_p)$ on sets of wave vectors $\boldsymbol{k}_p$, to impose Bragg-like peaks at arbitrary continuous positions. When choosing minimal sets of $\boldsymbol{k}_p$ with specific discrete rotational symmetries that are not attainable with simple crystals [29], we observe the emergence of a full quasicrystalline structure, which we now investigate.

VI. QUASICRYSTALLINE STRUCTURES

In Fig. 6, we explore more discrete symmetries. Instead of imposing repulsive interactions, we repeat several cycles of FReSCo minimization, removing at each iteration points that overlap exactly with others, and replace them with new points drawn uniformly in a box $[-L/2; L/2]^d$, maintaining total occupancy N. For $N \approx 10\,000$ points in $2d$, imposing 8-, 10-, or 12-fold symmetries leads to point patterns with quasicrystalline characteristics [27], namely aperiodicity in real space (second column), and a peaked structure factor (third column). We also show that, like quasicrystals [45], our structures display strong local bond-orientational order, as can be seen from the $2d$ histograms of nearest neighbor vectors

(third column), that feature very narrow peaks, a sign that the long-range orientational order from our constraints reach all the way down to short ranges (see SM [35] for additional data).

Likewise, we show (last two rows) that we can impose icosahedral or dodecahedral peak arrangements in $3d$. Like previously reported $3d$ quasicrystals, they display five- and sixfold aperiodic orders in projected views [45] (second column), with associated peaked structure factors [27] (third column) and peaked nearest-neighbor vector distributions on the sphere, here shown as stereographic projections (fourth column). We show additional projections for these $3d$ structures in SM [35], highlighting that icosahedral and dodecahedral structures display similar rotational symmetry axes in spite of their different local structure, as they are dual of one another. For all structures, we also show (rightmost column) that we observe the expected anisotropic transmission patterns of quasicrystalline structures [7]. It is interesting that imposing only n peaks of intensity $O(N)$ with the right symmetry around the origin in Fourier space is sufficient to obtain quasicrystalline order. Indeed, as discussed in Appendix H, imposing a peak of intensity N at specific wav vectors in $S(\boldsymbol{k})$ implies that integer-coefficient linear combinations of these wave vectors will also have N-high peaks, but the most intense quasicrystalline peaks are in general not strictly N high, just $O(N)$ [27], so that the constraint on linear combinations is
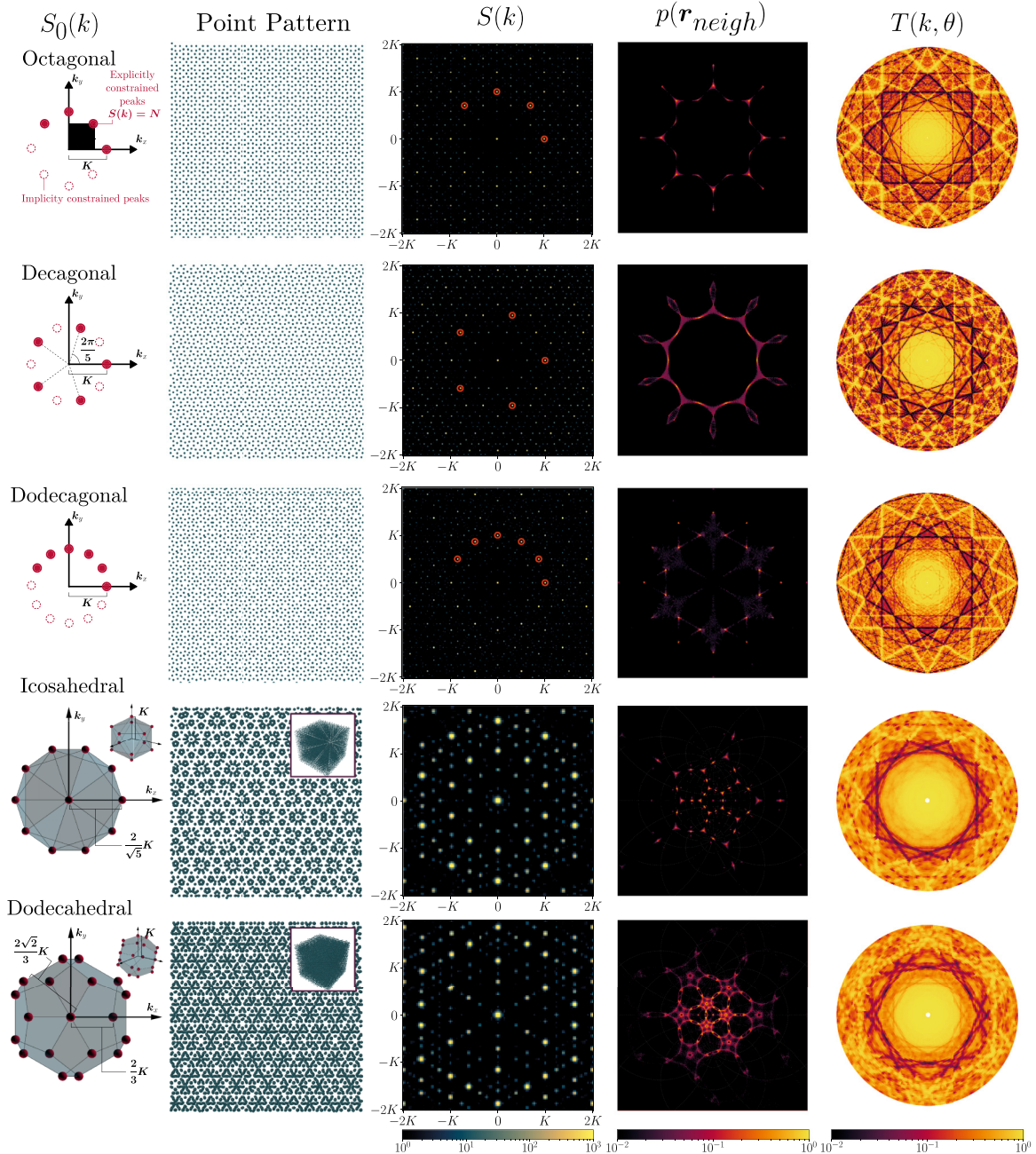
FIG. 6. Generation of special symmetries using NUwNU. From left to right, sketches of the constrained peaks in $S(k)$, portion of the output point pattern, intensity map of the structure factor, density map of the distribution of Voronoi nearest neighbors, and Ewald transmission plot (all in log-intensity) for systems of $N \approx 10^4$ particles constrained with NUwNU to maximize peak height at specific locations in k space. Each row shows one specific type of imposed n-fold symmetry: From top to bottom, we show 8-fold, 10-fold, and 12-fold symmetry in $2d$, then icosahedral and dodecahedral peak arrangements in $3d$. In the structure factor, we highlight constrained peaks in $2d$. In $3d$, we replace the $2d$ panels by close equivalents. The point patterns are projected onto the xy plane, orthogonal to a long diagonal of the polyhedra (the full system is shown in inset), and the structure factor is accordingly in the $k_z = 0$ plane, where we highlight the lowest-order, implicitly constrained, peaks, and the Ewald construction is obtained by scanning only xy (azimuthal) orientations. The full distribution of Voronoi nearest neighbors is replaced by the distribution of bond orientations to nearest neighbors on a stereographic projection of the sphere.

much weaker. Our optimization approach thus enables the *nondeterministic* generation of aperiodic structures with custom photonic properties and free boundary conditions. This dramatically expands the design space for aperiodic structures, heretofore mostly limited to *deterministic* examples, e.g., to promote Anderson localization [46].

VII. ITERATIVE CONSTRAINTS FOR ADAPTIVE SAMPLING

Finally, our approach provides a way of designing optimal sampling strategies for Monte Carlo integrations, as the spectral content of a point pattern directly determines their mean-square error [12]. So far, a lot of attention has been

devoted to blue noise, often in the form of stealthy hyperuniform point patterns, for integration [10,12,47–50]. However, for applications such as real-time rendering of dynamical virtual scenes, it is essential to generate adaptive point patterns that have suitable properties in terms of both spatial and temporal correlations to effectively handle motion [11,51].

FReSCo, with its remarkable speed, provides an effective tool to address this problem. To demonstrate this, we impose approximately 800 frames from a Lumière film [52] as a sequence of structure factor constraints $S_0(k)$. Specifically, by using the point pattern for frame i as the initial condition for the subsequent minimization at frame $i + 1$, we encode the film in trajectories of $N = 300\,000$ points in $2d$ (see video in SM [35] and Appendix I for further details).

VIII. CONCLUSIONS

We have demonstrated a highly efficient generative algorithm, FReSCo, that precisely embeds k-space features into point patterns up to previously inaccessible scales and that can be combined to short-range interactions like excluded volume. This paves the way to exploring novel wave transport properties, like new structurally colored coatings [5]. Future work will focus on the systematic characterization of large-scale structures designed by FReSCo at the multiple scattering level, thus enabling a comprehensive analysis of the factors that give rise to photonic band gaps and Anderson localization in correlated disordered media [8,9,20]. As only a handful of systems have been studied so far, our approach paves the way for the discovery of yet unknown structures with these properties.

More generally, one may impose more complicated real-space interactions—e.g., constraints onto the real-space pair correlation function like in reverse Monte Carlo [53] [see Appendix B for a formulation of FReSCo that optimizes the real-space pair correlation function $g(\mathbf{r})$] or potentials that favor local orientational order (such as three-body terms, e.g., Stillinger-Weber-type potentials [54]). These extensions would clarify the role of local orientational order in wave transport [4,36] and facilitate fabrication, as tetrahedral order is often imposed *a posteriori* [6,36,37]. Our algorithm may be generalized to include higher-order correlations, for instance three- and four-body correlations that are also computable in $\mathcal{O}(N \log N)$ using FFTs [55]. Furthermore, using automatic differentiation [56], our loss can guide the design of interactions realizing the self-assembly of spectrally shaped structures.

Finally, the fast optimization provided by FReSCo could have a significant impact on real-time rendering relying on Monte Carlo integration.

ACKNOWLEDGMENTS

APPENDIX A: ALGORITHM PARAMETERS

The size of the domain in which the optimization is performed, $\mathcal{N}_K = |\mathcal{K}|$, counted in number of discrete wave vectors, is limited in practice by the number of degrees of freedom, dN, for N points embedded in d-dimensional space. This constraint often leads to defining a ratio $\chi \equiv \mathcal{N}_K/[2d(N-1)]$ [9,16–18], where the two stems from Friedel's law and the $N - 1$ come from removing global translations from the available degrees of freedom, as S is translation invariant. Optimizations with $\chi < 1$ are in theory possible, while those with $\chi \geqslant 1$ are overconstrained and cannot necessarily be achieved [68]. Past work has also shown using other algorithms that, even for $\chi < 1$, high values of χ lead to large changes in S beyond the constrained region, going as far as near-crystallization [16]. In practice, these effects remain weak using $\chi \lesssim 0.5$ [16] in $2d$ space. In this work, we always set $\chi \approx 0.4$, so that the number of constrained k-space features scales linearly with N.

The bulk of the computations consists of Fourier transforms between uniform and nonuniform spaces [Fig. 1(a)]. We use the FINUFFT framework which provides transforms of three types and is highly optimized for multithreaded CPU computations [30,31]. Type-1 refers to a nonuniform to uniform transform [e.g., real space points to a k-space grid as used in the calculation of the structure factor in Eq. (1)]. Type-2 refers to a uniform to nonuniform transform [e.g., k-space grid to known points in real space as used in the calculation of the loss gradient in Eq. (4)]. Type-3 refers to a nonuniform to nonuniform transform (e.g., real space points to specific points in k space, with free boundary conditions, as used in the calculation of the Ewald sphere or in NUwNU, see below).

The termination criterion for optimization throughout the text was a threshold value of 10^{-39} on the gradient. In the special case of stealthy hyperuniform systems, this criterion achieves low-k values, $S \sim 10^{-25}$–10^{-20}. Lower values such as those reported in Ref. [18] can be attained within the powerful framework of FReSCo using a different termination value and higher precision arithmetics, but such small values are not realistic in any practical realization (see Appendix E for a detailed discussion of this point).

APPENDIX B: ANALYTICAL GRADIENTS

We here show how one may write the gradient of the structure factor loss, $\mathcal{L}_S$, analytically as a Fourier series for all four constructions UwU, UwNU, NUwU, and NUwNU. In Eq. (1) we introduced the structure factor

$$S(\boldsymbol{k}) \equiv \frac{|\widehat{\rho}(\boldsymbol{k})|^2}{N}$$

associated to a d-dimensional density field describing N points with complex-valued weights $(c_1, \ldots, c_N)$ at positions $(r_1, \ldots r_N)$ in $\mathbb{R}^d$,

$$\rho(\boldsymbol{r}) = \sum_{n=1}^{N} c_n \delta(\boldsymbol{r} - \boldsymbol{r}_n), \tag{B1}$$

through its Fourier transform,

$$\widehat{\rho}(\boldsymbol{k}) = \sum_{n=1}^{N} c_n \exp(i\boldsymbol{k} \cdot \boldsymbol{r}_n). \tag{B2}$$

For simplicity, in the following, we absorb the normalization by S_0 in Eq. (3) into the weighting function $W(\boldsymbol{k}) = w(\boldsymbol{k})/S_0(\boldsymbol{k})^2$ if $S_0(\boldsymbol{k}) \neq 0$ and $W(\boldsymbol{k}) = w(\boldsymbol{k})$ otherwise, so that at every point we can rewrite the loss, Eq. (2), as

$$\mathcal{L}_S = \sum_{\boldsymbol{k} \in \mathcal{K}} W(\boldsymbol{k})[S(\boldsymbol{k}) - S_0(\boldsymbol{k})]^2. \tag{B3}$$

We first restrict ourselves to the case of real-valued weights and write the gradient of this loss with respect to one of the weights, $c_n \in \mathbb{R}$, corresponding to the optimization of a real-valued field at fixed mesh positions,

$$\frac{\partial \mathcal{L}_S}{\partial c_n} = \sum_{\boldsymbol{k} \in \mathcal{K}} 2W(\boldsymbol{k})[S(\boldsymbol{k}) - S_0(\boldsymbol{k})] \frac{\partial S(\boldsymbol{k})}{\partial c_n}. \tag{B4}$$

The corresponding derivative of the Fourier transform of the density field, Eq. (B2), then reads

$$\frac{\partial \widehat{\rho}(\boldsymbol{k})}{\partial c_n} = e^{i\boldsymbol{k} \cdot \boldsymbol{r}_n}, \tag{B5}$$

Recalling that, in general, the structure factor can be written as

$$S(\boldsymbol{k}) = |\widehat{\rho}(\boldsymbol{k})|^2/\rho_0 = \widehat{\rho}(\boldsymbol{k})\widehat{\rho}^{\dagger}(\boldsymbol{k})/\rho_0, \tag{B6}$$

where $\rho_0 = \sum_j |c_j|^2$, we may write the gradient components of S as:

$$\frac{\partial S}{\partial c_n} = \frac{1}{\rho_0}[\widehat{\rho}^{\dagger}(\boldsymbol{k})e^{i\boldsymbol{k} \cdot \boldsymbol{r}_n} + \widehat{\rho}(\boldsymbol{k})e^{-i\boldsymbol{k} \cdot \boldsymbol{r}_n}] - \frac{2c_n|\widehat{\rho}(\boldsymbol{k})|^2}{\rho_0^2}. \tag{B7}$$

The first two terms in this expression may be simplified by noticing that they are the sum of a number with its conjugate, so that

$$\frac{\partial S}{\partial c_n} = \frac{2}{\rho_0}\text{Re}[\widehat{\rho}(\boldsymbol{k})e^{-i\boldsymbol{k} \cdot \boldsymbol{r}_n}] - \frac{2c_n}{\rho_0}S(\boldsymbol{k}). \tag{B8}$$

Injecting this expression into Eq. (B4), one may find that the gradient can be calculated by taking the real part of a Fourier transform:

$$\frac{\partial \mathcal{L}_S}{\partial c_n} = \text{Re}\left[\sum_{\boldsymbol{k} \in \mathcal{K}} \boldsymbol{C}_{c_n}(\boldsymbol{k})e^{-i\boldsymbol{k} \cdot \boldsymbol{r}_n}\right] - \boldsymbol{F}_{c_n} = \text{Re}[\widehat{\boldsymbol{C}}_{c_n}(\boldsymbol{r}_n)] - \boldsymbol{F}_{c_n}, \tag{B9}$$

where $\boldsymbol{C}_{c_n}(\boldsymbol{k}) = 4W(\boldsymbol{k})[S(\boldsymbol{k}) - S_0(\boldsymbol{k})]\widehat{\rho}(\boldsymbol{k})/\rho_0$ are coefficients of a Fourier series, $\widehat{\boldsymbol{C}}_{c_n}$ is the Fourier transform of $\boldsymbol{C}_{c_n}$, and $\boldsymbol{F}_{c_n} = \frac{4c_n}{\rho_0}\sum_{\boldsymbol{k} \in \mathcal{K}} W(\boldsymbol{k})S(\boldsymbol{k})[S(\boldsymbol{k}) - S_0(\boldsymbol{k})]$.

Likewise, we write the gradient of the loss with respect to one of positions, $\boldsymbol{r}_n$, corresponding to the optimization of

continuous positions with fixed complex weights,

$$\frac{\partial \mathcal{L}_S}{\partial \boldsymbol{r}_n} = \sum_{\boldsymbol{k} \in \mathcal{K}} 2W(\boldsymbol{k})[S(\boldsymbol{k}) - S_0(\boldsymbol{k})] \frac{\partial S(\boldsymbol{k})}{\partial \boldsymbol{r}_n}. \tag{B10}$$

Using the definition of S again, coupled with the derivative of the Fourier transform of the density field:

$$\frac{\partial \widehat{\rho}(\boldsymbol{k})}{\partial \boldsymbol{r}_n} = i\boldsymbol{k}c_n e^{i\boldsymbol{k} \cdot \boldsymbol{r}_n}, \tag{B11}$$

the gradient components of S can be recast as

$$\frac{\partial S}{\partial \boldsymbol{r}_n} = \frac{i\boldsymbol{k}}{N}[c_n\widehat{\rho}^{\dagger}(\boldsymbol{k})e^{i\boldsymbol{k} \cdot \boldsymbol{r}_n} - c_n^{\dagger}\widehat{\rho}(\boldsymbol{k})e^{-i\boldsymbol{k} \cdot \boldsymbol{r}_n}]. \tag{B12}$$

Once again, this expression may be simplified by noticing that it is the sum of a number with its conjugate, so that

$$\frac{\partial S}{\partial \boldsymbol{r}_n} = 2\text{Re}\left[-\frac{i\boldsymbol{k}c_n^{\dagger}}{N}\widehat{\rho}(\boldsymbol{k})e^{-i\boldsymbol{k} \cdot \boldsymbol{r}_n}\right]. \tag{B13}$$

Injecting this expression into Eq. (B10), one recovers Eq. (4) of the main text:

$$\frac{\partial \mathcal{L}_S}{\partial \boldsymbol{r}_n} = \text{Re}\left[\sum_{\boldsymbol{k}} \boldsymbol{C}_{r_n}(\boldsymbol{k})c_n^{\dagger} \exp(-i\boldsymbol{k} \cdot \boldsymbol{r}_n)\right] = \text{Re}[c_n^{\dagger}\widehat{\boldsymbol{C}}_{r_n}(\boldsymbol{r}_n)], \tag{B14}$$

where $\boldsymbol{C}_{r_n}(\boldsymbol{k}) = -4i\boldsymbol{k}w(\boldsymbol{k})[S(\boldsymbol{k}) - S_0(\boldsymbol{k})]\widehat{\rho}(\boldsymbol{k})/N$ are coefficients of a Fourier series, and $\widehat{\boldsymbol{C}}_{r_n}$ is the Fourier transform of $\boldsymbol{C}_{r_n}$.

From Eqs. (B9) and (B14), we define four variants of our optimization algorithm depending on the structure of k-space constraints and of the density field that are considered. While it is in principle possible to simultaneously optimize weights and nonuniform positions, we leave that possibility for future work and only consider optimization of either weights or positions.

1. UwU: Uniform real space with uniform k-space constraints

First, consider the case of a density field constrained to a square grid, also called a *uniform* sampling of space [11]. In that case, one may optimize the weights at each point so as to obtain a square-grid meshing of a field with desirable correlations. In particular, if the system is defined with periodic boundary conditions, then one may impose features at $\boldsymbol{k}$ vectors also lying on a grid or in other words use a *uniform* constraint. We therefore call this variant UwU, uniform real space density with uniform k-space constraints. Since both the real-space density field and the Fourier-space constraints are uniform, this is the only scenario in which one may compute both the loss and its gradient with usual discrete Fourier transform algorithms.

2. UwNU: Uniform real space with nonuniform k-space constraints

Consider the case of a uniform density field, but with free boundary conditions, so that one may impose nonuniform Fourier constraints at arbitrary continuous positions, or UwNU. This case (UwNU) utilizes one FINUFFT Type-2 transformation (uniform to nonuniform) to calculate $S(\boldsymbol{k})$ and

one FINUFFT Type-1 transformation (nonuniform to uniform) to calculate the gradient of the loss.

3. NUwU: Nonuniform real space with uniform k-space constraints

If we now optimize real-space positions, resulting in a nonuniform set of real positions with periodic boundary conditions, and therefore use uniform Fourier-space constraints, then we get NUwU. This case (NUwU) utilizes one FINUFFT Type-1 transformation (nonuniform to uniform) to calculate $S(\boldsymbol{k})$ and d FINUFFT Type-2 transformations (uniform to nonuniform) to calculate the gradient of the loss (one for each dimension of $\boldsymbol{k}$).

4. NUwNU: Nonuniform real space with nonuniform k-space constraints

Finally, we may optimize nonuniform real-space positions, but this time with free boundary conditions, leading to arbitrary nonuniform Fourier-space constraints and to NUwNU. This case (NUwNU) utilizes one FINUFFT Type-3 transformation (nonuniform to nonuniform) to calculate $S(\boldsymbol{k})$ and d additional FINUFFT Type-3 transformations to calculate the gradient of the loss (one for each dimension of $\boldsymbol{k}$).

5. Pair correlation function optimization

Our optimization strategy can be generalized to optimize the real-space pair correlation function $g(\boldsymbol{r})$. For a real-valued density field generated by a spatially uniform process inside a cubic box with sidelength L, the pair correlation function is defined [28] as

$$g(\boldsymbol{r}) \equiv L^d \frac{\int d^d\boldsymbol{r}_1 d^d\boldsymbol{r}_2 \rho(\boldsymbol{r}_1)\rho(\boldsymbol{r}_2)\delta(\boldsymbol{r}-\boldsymbol{r}_{12})}{(\int d^d\boldsymbol{r}_1 \rho(\boldsymbol{r}_1))(\int d^d\boldsymbol{r}_2 \rho(\boldsymbol{r}_2))}, \qquad \text{(B15)}$$

which tends to 1 as the density fields at positions $\boldsymbol{r}_1$ and $\boldsymbol{r}_1 + \boldsymbol{r}$ become independent, usually as $r \to \infty$. This expression can be simplified using the definition of the density field of a point pattern, and excluding the $i = j$ point from the sum per the usual convention [28], yielding

$$g(\boldsymbol{r}) = \frac{L^d}{N^2\overline{c_n}^2} \sum_{i\neq j} c_i c_j \delta(\boldsymbol{r}-\boldsymbol{r}_{ij}), \qquad \text{(B16)}$$

where we defined the arithmetic average of the weights, $\overline{c_n} \equiv \sum_n c_n/N$. This last expression can be written as an inverse Fourier transform of $S(\boldsymbol{k}) - 1$, namely

$$g(\boldsymbol{r}) = \frac{1}{n_0\overline{c_n}^2} \int_{\mathcal{F}} \frac{d^d\boldsymbol{k}}{(2\pi)^d}[S(\boldsymbol{k})-1]e^{-i\boldsymbol{k}\cdot\boldsymbol{r}}, \qquad \text{(B17)}$$

where the integral is computed over the whole Fourier domain $\mathcal{F}$ and n_0 is the spatially averaged number density, $n_0 = N/L^d$. Note that in the standard setting of liquid theory, $\forall n, c_n = 1$ so that the prefactor simply becomes $1/n_0$, yielding the more usual relation between S and g [28]. For compactness, we henceforth define $\rho_0 = n_0\overline{c_n}^2$.

The associated loss term can be written as a sum over a discrete set $\mathcal{R}$ of constrained real-space distances $\boldsymbol{x}$ instead of

reciprocal-space wave vectors,

$$\mathcal{L}_g \equiv \sum_{\boldsymbol{x}\in\mathcal{R}} W_g(\boldsymbol{x})[g(\boldsymbol{x})-g_0(\boldsymbol{x})]^2, \qquad \text{(B18)}$$

where W_g is a weight function that can for instance select short-range order to be jointly optimized with some longer-range property in S. The gradient of this loss term with respect to the position $\boldsymbol{r}_n$ of particle n can be expressed as

$$\frac{\partial\mathcal{L}_g}{\partial\boldsymbol{r}_n} = \sum_{\boldsymbol{x}\in\mathcal{R}} 2W_g(\boldsymbol{x})[g(\boldsymbol{x})-g_0(\boldsymbol{x})]\frac{\partial g}{\partial\boldsymbol{r}_n}(\boldsymbol{x}). \qquad \text{(B19)}$$

Since we optimize structures in finite periodic boxes, the integral in Eq. (B17) reduces to a discrete Fourier transform,

$$g(\boldsymbol{r}) = \mathrm{Re}\left\{\frac{V_k}{\rho_0}\sum_{\boldsymbol{k}}[S(\boldsymbol{k})-1]e^{-i\boldsymbol{k}\cdot\boldsymbol{r}}\right\}, \qquad \text{(B20)}$$

where $V_k = (1/L)^d$ is the discretization volume used when switching to a discrete Fourier transform. As a result, one may express the gradient of g with respect to the position $\boldsymbol{r}_n$ of particle n as

$$\frac{\partial g}{\partial\boldsymbol{r}_n}(\boldsymbol{x}) = \mathrm{Re}\left[\frac{V_k}{\rho_0}\sum_{\boldsymbol{k}}\frac{\partial S(\boldsymbol{k})}{\partial\boldsymbol{r}_n}e^{-i\boldsymbol{k}\cdot\boldsymbol{x}}\right]. \qquad \text{(B21)}$$

The gradient of $\mathcal{L}_g$ can then be expressed as

$$\frac{\partial\mathcal{L}_g}{\partial\boldsymbol{r}_n} = \frac{2V_k}{\rho_0}\mathrm{Re}\left\{\sum_{\boldsymbol{k}}\frac{\partial S(\boldsymbol{k})}{\partial\boldsymbol{r}_n}\sum_{\boldsymbol{x}\in\mathcal{R}}W_g(\boldsymbol{x})[g(\boldsymbol{x})-g_0(\boldsymbol{x})]e^{-i\boldsymbol{k}\cdot\boldsymbol{x}}\right\}. \qquad \text{(B22)}$$

Finally, one may define

$$G(\boldsymbol{k}) \equiv 2\sum_{\boldsymbol{r}\in\mathcal{R}} W_g(\boldsymbol{x})[g(\boldsymbol{x})-g_0(\boldsymbol{x})]e^{-i\boldsymbol{k}\cdot\boldsymbol{x}} \qquad \text{(B23)}$$

such that

$$\frac{\partial\mathcal{L}_g}{\partial\boldsymbol{r}_n} = \frac{V_k}{\rho_0}\mathrm{Re}\left[\sum_{\boldsymbol{k}}\frac{\partial S(\boldsymbol{k})}{\partial\boldsymbol{r}_n}G(\boldsymbol{k})\right]. \qquad \text{(B24)}$$

All in all, introducing the weight c_n of each point again,

$$\frac{\partial\mathcal{L}_g}{\partial\boldsymbol{r}_n} = -\frac{2V_k}{\rho_0 N}\mathrm{Re}\left[\sum_{\boldsymbol{k}} i\boldsymbol{k}c_n^\dagger\rho(\boldsymbol{k})G(\boldsymbol{k})e^{-i\boldsymbol{k}\cdot\boldsymbol{r}_n}\right]. \qquad \text{(B25)}$$

This last expression can be evaluated using two Fourier transforms. As Eqs. (B20) and (B25) can be evaluated using regular FFTs, the loss minimization in $g(\boldsymbol{r})$ may thus be performed in $\mathcal{O}(N\log N)$ time as well (per iteration).

In Fig. 7, we show an example output of this strategy, using $g_0(r \leqslant \sigma) = 0$ as a target and 2001×2001 Fourier modes in an $N = 10\,000$ point pattern with σ an exclusion diameter. The result does exhibit a hard-disk-like structure factor [Fig. 7(b)] and pair correlation function [Fig. 7(c)], although it is less ordered than equilibrium hard disks, as highlighted by the comparison to Percus-Yevick curves. This indicates that our optimization does *not* sample hard disk configurations uniformly like equilibrium simulations would. Note, however, that, due to the finite number of modes, the evaluation of g via an inverse Fourier transformed displays aliasing errors: A perfect step function cannot be represented
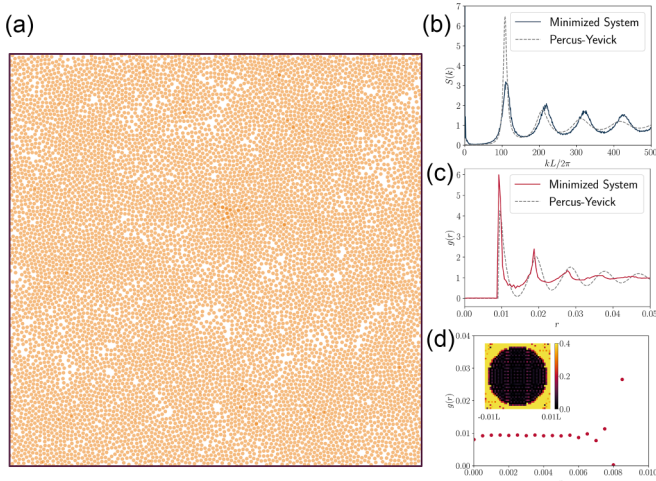
FIG. 7. Constraining the pair correlation function $g(r)$ using modified NUwU. (a) A point pattern obtained by constraining $g_0(r < \sigma) = 0$ for an exclusion diameter σ such that $\phi = 0.7$. Disks are drawn with diameter σ with transparency to highlight overlaps remaining in the final system. (b) The radial structure factor of the point pattern (solid line) compared to the structure factor of the Percus-Yevick solution for ideal hard disks (dashed line). (c) The pair correlation function of the point pattern calculated using radial binning, compared with the Percus-Yevick prediction. (d) A zoomed in portion of the pair correlation function used during minimization (calculated using the Fourier transform of the structure factor). Due to the Fourier transform using only a finite number of modes, the $g(r)$ that is used to minimize exhibits aliasing, resulting in imperfect minimization.

with any finite number of Fourier modes, leading to rippling [11]. In Fig. 7(d), we highlight this by showing a zoom onto the early values of the final $g(r)$, which is not exactly zero [this can also be seen in Fig. 7(a) in the form of a small number of overlaps]. In the inset, we show the corresponding zoom onto the center of the 2d $g(\mathbf{r})$, which shows that these overlaps actually lie on a discrete grid due to aliasing. Note that this issue is likely to be worse in sharp features like the hardcore repulsion we show here but should not be as much of an issue when imposing smoother features, i.e., features with less high-frequency content (ideally band-limited features).

APPENDIX C: UNIFORM FIELDS WITH k-SPACE CONSTRAINTS (UwU and UwNU)

While our work focuses on nonuniform real space systems (i.e., point patterns), our methodology is easily extendable to uniform systems (e.g., discretized density fields) using the same tools. Using the UwU and UwNU protocols, we can generate density fields with k-space properties analogous to those of point patterns we have shown elsewhere in this paper (Fig. 8). It is important to note that, in the UwU case, the k space is exactly as large as the real space. If one were to fully constrain k space (i.e., constrain both the complex phase and magnitude of $\widehat{\rho}(\mathbf{k})$ at every grid coordinate), then a single inverse Fourier transform could be used to find a corresponding real space structure rather than a minimization protocol.

However, UwU as defined in this paper only constrains the structure factor [i.e., the modulus $|\widehat{\rho}|(\mathbf{k})$] over a set of wave vectors that does not have to cover the whole system. It may therefore be used to find uniform real space systems with complete freedom over the phase degree of freedom, and underconstrained power spectra, such as those depicted in Fig. 8. In particular, this could be used to generate first guesses to initialize phase retrieval algorithms in the context of image reconstruction, see, e.g., Refs. [42,69], to generate textures with suitable properties [43,70], or to generate discretized versions of random fields with suitable correlations [44].

Furthermore, UwNU can be used to impose peaked features at continuous values onto uniform systems with free boundary conditions: This could, for instance, be useful to generate nonrepeating random textures. In Fig. 8, we illustrate UwNU by constraining six peaks forming a hexagon as well as the central peak, such that they are all $O(N)$ with N the number of pixels of the real field. As the radius of the hexagon is varied, we see that the field forms various valid lattices of the triangular family that feature a hexagon of like-valued peaks: namely a triangular lattice (first and third row from the top) and a Kagome-like structure composed of triangular-shaped peaks forming a honeycomb lattice (second and fourth row). These fields are all valid solutions for our constraint here as, unlike in NUwNU, the number and the spatial extents of real-space peaks are not constrained.

APPENDIX D: BENCHMARK OF FReSCo

We collect data for full minimization ("wall") times elapsed during the generation of stealthy disordered hyperuniform point patterns, power-law hyperuniform point patterns, and power-law hyperuniform disk or sphere packings in 2d and 3d, all starting from independent Poisson point processes (Fig. 9). Point patterns were minimized to a root-mean-square error of 10^{-39} on the gradient, while particle packings were minimized to a root-mean-square error of 10^{-10} on the gradient, using L-BFGS [32] with a maximal step size and a backtracking line search [33]. All systems demonstrate large-N scaling very near $N \log N$ for total times (dashed black lines) as the system size increases. Note that this scaling is observed for full minimization procedures, which is a stronger result than the scaling of individual iterations, that is, $N \log N$ by definition.

To emphasize this point, we also show the number of required iterations as a function of N. Since a single minimization step is guaranteed to scale like $\mathcal{O}(N \log N)$, the overall scaling is that of the number of function evaluations multiplied by $N \log N$. Therefore, we want to show that the number of function evaluations, n_{ev}, is sublinear in N to demonstrate that FReSCo overall outperforms previous N^2 or N^3 algorithms. We show that the scalings are systematically sublinear for all tested systems, with scalings $n_{\mathrm{ev}} \lesssim O(N^{\frac{1}{5}})$ for stealthy hyperuniform point patterns, $n_{\mathrm{ev}} \lesssim O(N^{\frac{1}{8}})$ for power-law hyperuniform point patterns, and $n_{\mathrm{ev}} \lesssim O(N^{\frac{1}{2}})$ for power-law hyperuniform particle packings. All minimizations were here performed on a single CPU node (a 24-core Intel
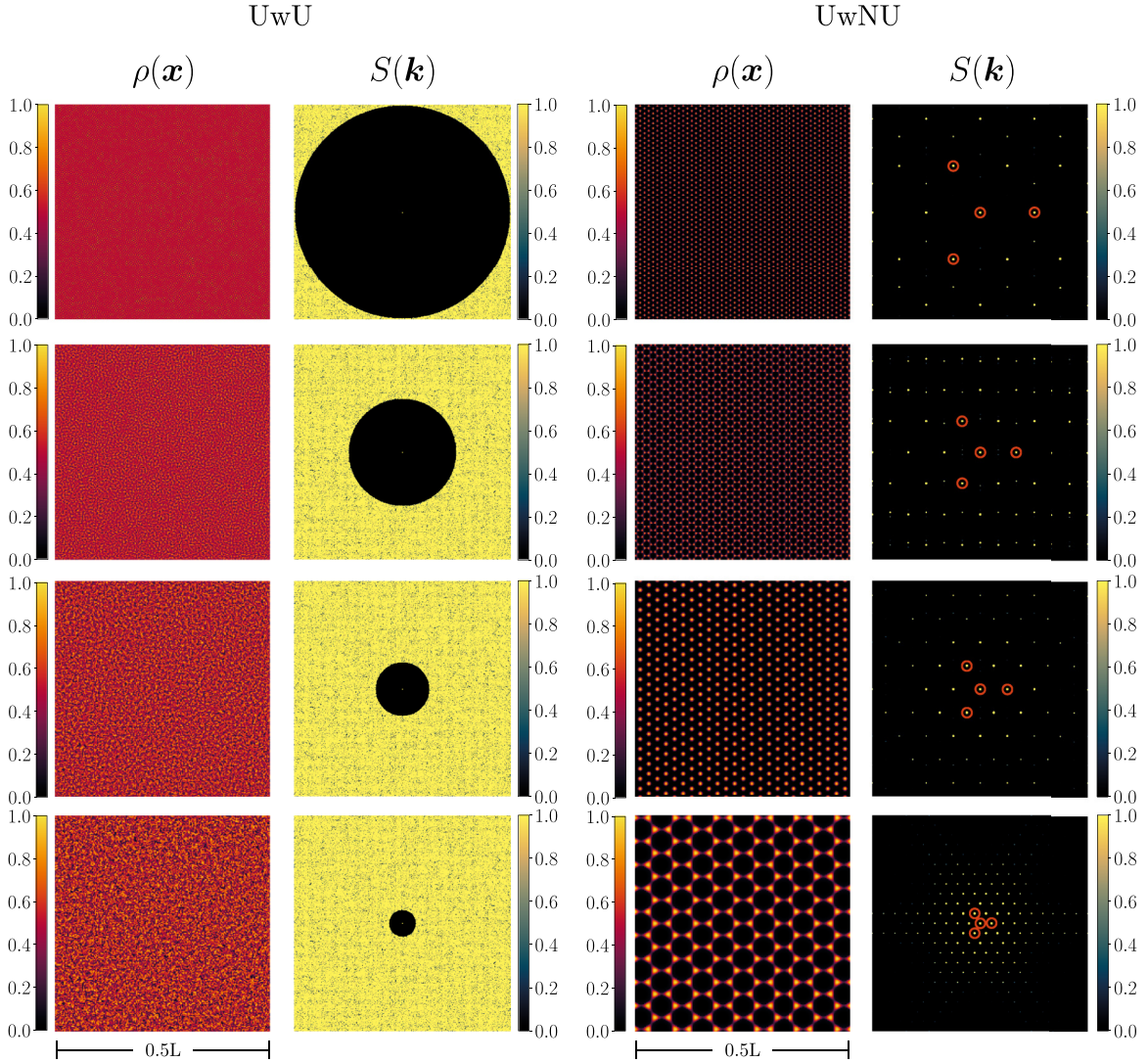
FIG. 8. Example systems generated using UwU (left) and UwNU (right). Density fields of 403×403 are generated using UwU (left) and UwNU (right) protocols. UwU (left) systems are generated to exhibit varying degrees of stealthiness, as demonstrated in the varying radius of $S(k) = 0$ in the structure factor. The larger the radius, the more uniform the system appears. UwNU (right) systems are generated to exhibit sixfold symmetry, imposing only the peaks of the innermost hexagon (marked with red circles). As the radius of the innermost hexagon or peaks changes, we sometimes get a Kagome-like tiling instead of a triangular lattice.

Cascade Lake Platinum 8268 chip), parallelized over multiple cores. The number of cores used for all systems of Fig. 9 are given in detail in Table I.

APPENDIX E: ROBUSTNESS OF STEALTHY HYPERUNIFORMITY AGAINST NOISE

One of the main motivations for using disordered material structures in applications such as photonics where crystalline structures already perform well is that disordered structures can be more resilient to defects. Here we take minimized point patterns ($N = 5 \times 10^7$) and displace each point using a Gaussian random normal distribution of mean $\mu = 0$ and standard deviation $\sigma = L\delta/N^{\frac{1}{d}}$, where δ is a fraction of the average interparticle distance (Fig. 10). Doing so, one expects the new low-k structure factor to be, at every point, the maximum of the power spectrum of the noise (which here grows

like k^2) and of the original structure factor [71]. In the stealthy hyperuniform case, we show that, although we are able to minimize the structure factor down to a magnitude of $\sim 10^{-24}$ at its minimum value, it only takes a noise corresponding to $\delta = 10^{-9}$ to raise that value. For the case of a $N = 5 \times 10^7$ point pattern, this δ value results in a standard deviation of $\sigma \approx 1.4 \times 10^{-13}L$, which implies that the noise level would be equivalent to sub-Angstrom displacements in a $L = 1$ km size device with typical interparticle spacing $d \approx 10$ cm. In practice, the difference in $S(k)$ magnitude between, say, 10^{-6} and 10^{-24} is irrelevant for any realistic fabrication process. Furthermore, most practical applications likely do not need such high precision in $S(k)$ in practice. We demonstrate this by showing the effect of Gaussian noise on a highly detailed structure factor (in linear intensity scale), namely a *The Starry Night* [23] structure factor point pattern ($N = 5 \times 10^7$). We observe that long-range correlations are well preserved up to
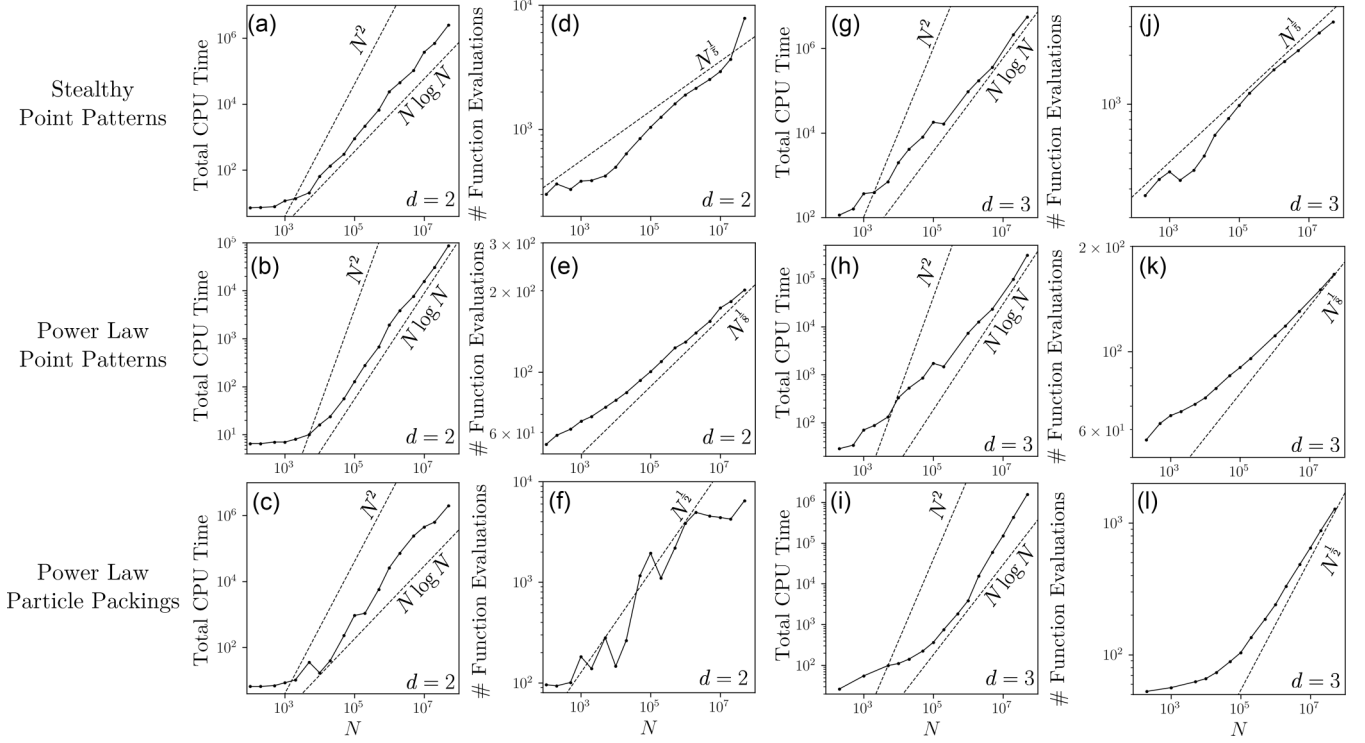
FIG. 9. Performance benchmarks. Total CPU time (in seconds) utilized for full minimization plotted against system size N in a log-log scale in $2d$ [(a)–(c)] and $3d$ [(g)–(i)]. Alongside, (d)–(f) and (j)–(l) are plots of the total number of function evaluations used to achieve the termination condition for minimization. Systems generated are stealthy disordered hyperuniform point patterns [(a) and (d) as well as (g) and (j)], power-law hyperuniform point patterns [(b) and (e) as well as (h) and (k)], and power-law hyperuniform disk or sphere packings [(c) and (f) as well as (i) and (l)]. On each plot of CPU time, a reference line representing $\mathcal{O}(N \log N)$ scaling is plotted for comparison, as well as the best-case scaling per iteration of previous methods $\mathcal{O}(N^2)$ (note that this does not take into account the scaling of number of evaluations in previous methods). On each plot of the number of function evaluations, an overestimate of the large-N scaling is plotted as a guide.

high values of the noise, while short-range correlations are washed out earlier. The effect of noise for $\delta = 0.1$ is only somewhat noticeable, corresponding to a standard deviation of $\sigma \approx 1.4 \times 10^{-5}L$. This implies that a $L = 1$ mm device with $d \approx 100$ nm distance between particles would be resilient to 10-nm-scale defects.

APPENDIX F: SIZE MATTERS: S AND NUMBER FLUCTUATION BEHAVIOR IN SMALL SYSTEMS

From each of the systems minimized for the benchmark in Fig. 9, we evaluate the reduced number variance $s^2 \equiv \langle N^2 \rangle / \langle N \rangle^2 - 1$, with averages performed over a set of circular
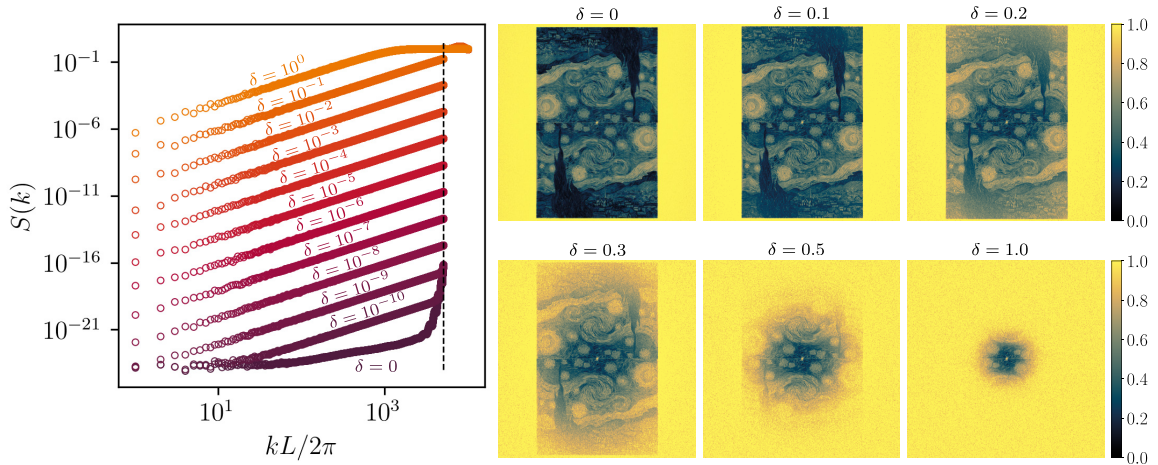
FIG. 10. Effect of Gaussian random noise on structure factor. Left: Angular averaged structure factors (log scale) of a $N = 5 \times 10^7$ stealthy hyperuniform point pattern subjected to varying degrees of Gaussian noise ($\sigma = L\delta/N^{\frac{1}{d}}$). Right: The $2d$ structure factor (linear scale) of a $N = 5 \times 10^7$ *The Starry Night* structure factor point pattern subjected to varying degrees of Gaussian noise ($\sigma = L\delta/N^{\frac{1}{d}}$).

TABLE I. Number of cores used for each system shown in the benchmark of Fig. 9.

N	No. cores (2d Points)	No. cores (2d Packings)	No. cores (3d Points)	No. cores (3d Packings)
10^2	2	2	2	2
2×10^2	2	2	2	2
5×10^2	2	2	2	2
10^3	2	2	4	4
2×10^3	2	2	4	4
5×10^3	2	2	4	4
10^4	4	4	8	4
2×10^4	4	6	8	4
5×10^4	8	8	8	4
10^5	12	12	12	4
2×10^5	12	16	12	4
5×10^5	12	24	12	4
10^6	24	32	24	4
2×10^6	24	32	24	4
5×10^6	24	48	24	6
10^7	24	48	48	8
2×10^7	24	48	48	12
5×10^7	48	48	48	24

or spherical sample volumes with radii $\ell \in [10^{-5}L, 0.5L]$ for 2d systems [Figs. 11(a)–11(f)] and $\ell \in [10^{-4}L, 0.5L]$ for 3d systems [Figs. 11(g)–11(l)]. We observe hyperuniform scaling for nearly four decades in 2d and at least two decades in 3d for systems containing $N = 5 \times 10^7$ points. In contrast, for our smallest systems, we only observe about one decade of hyperuniform scaling in 2d ($N = 100$) and less than one decade in 3d ($N = 200$). We note that the power-law scaling in the hyperuniform disk packing in Figs. 11(c)–11(f) appears to exhibit a broader crossover region, i.e., that follows neither of the asymptotic scalings, between the Poissonian scaling and the large-scale scaling imposed by the power law in $S(k)$. We believe this to be an effect of the treatment of the points as particles with pair repulsion at a somewhat high packing density $\phi = 0.6$, as we do not observe any deviation in the corresponding 3d case for a comparatively dilute packing fraction $\phi = 0.25$, Figs. 11(i) and 11(l).

APPENDIX G: EFFECT OF DETECTION WIDTH ON PERCEIVED TRANSMISSION GAPS

Throughout the text, we show results for T obtained by integrating over a full half-circle or half-sphere. In practice, any experimental result would be performed using a smaller
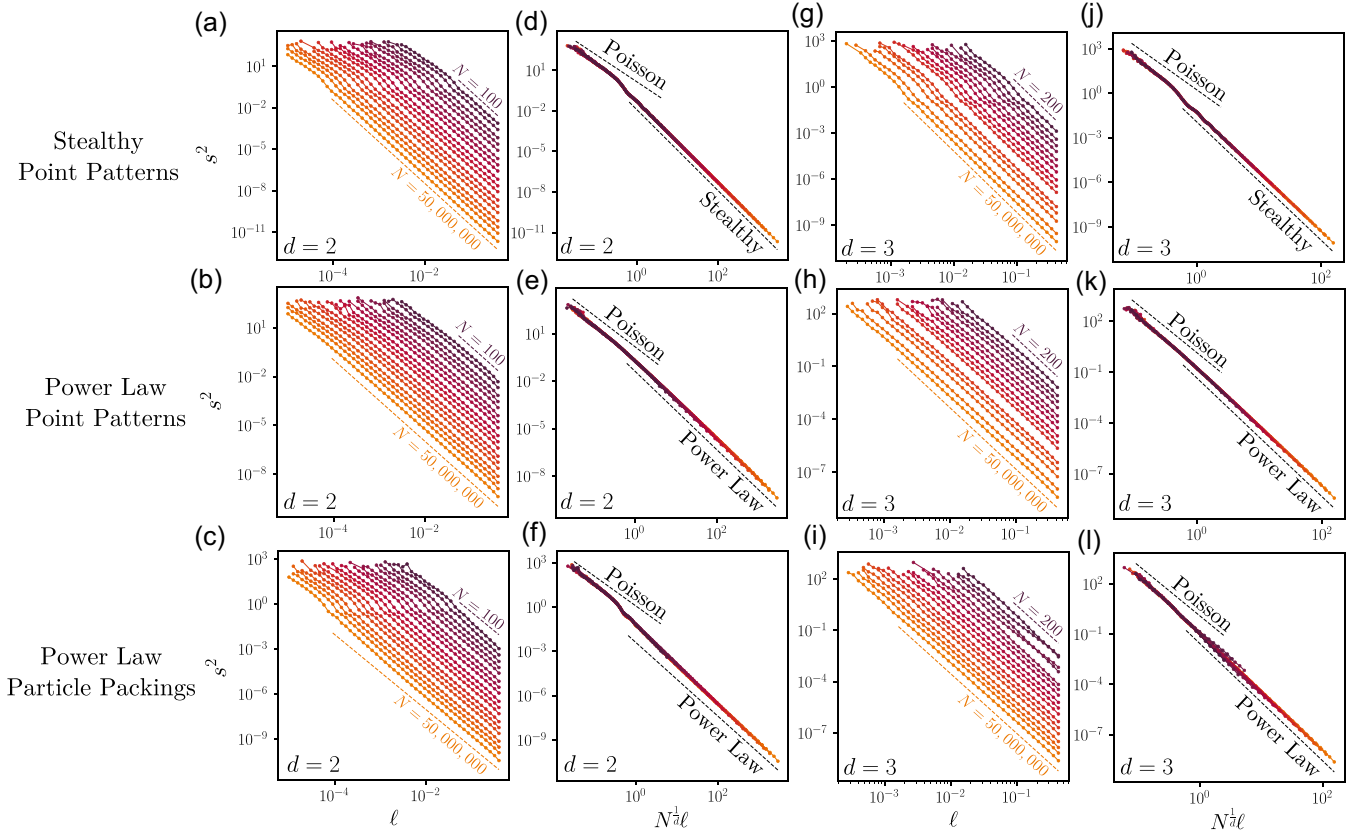
FIG. 11. Hyperuniform scaling across system sizes in 2d and 3d. Reduced number variance plots for stealthy disordered hyperuniform point patterns (top), power-law hyperuniform point patterns (middle), and power-law hyperuniform sphere packings (bottom). Plots on the left are plotted against the radius of the sample circle as a fraction of box length, showing a much narrower range of hyperuniform scaling in smaller systems. Plots on the right depict the data rescaled by $N^{\frac{1}{d}}$, showing the Poissonian scaling at short length scales transitioning to hyperuniform scaling at large length scales.
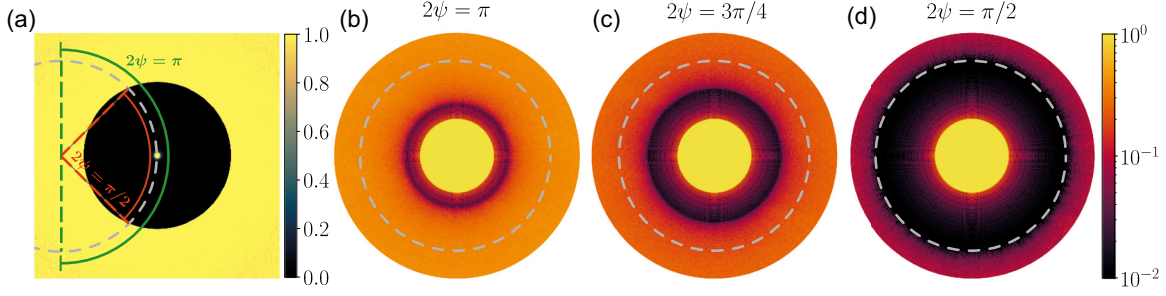
FIG. 12. Effects of varying aperture in stealthy hyperuniform systems. (a) Sketch of the effect of aperture in $2d$. Depending on the aperture angle $0 \leqslant 2\psi \leqslant \pi$ used for detection, the onset of forward scattering, and therefore the end of the transmission trough is observed at different frequencies. [(b)–(d)] Illustration: T obtained for a stealthy hyperuniform system ($N = 4 \times 10^7$, $K = 3000$), plotted up to $k_{\max} = 5000$, for $2\psi = \pi$ (b), $2\psi = 3\pi/4$ (c), and $2\psi = \pi/2$ (d). The dashed gray circle in panels (b)–(d) represents the same frequency as the one represented as a dashed gray circle in (a).

detection width, so that the integration domain $\mathcal{F}$ in the definition of T should be replaced by a finite angular region. We argue that this has a particular importance in the context of stealthy hyperuniform systems. To do so while preserving axial symmetry in the detection, we introduce a variant of T,

$$T_\psi(\boldsymbol{k}_{\mathrm{inc}}) \underset{3d}{\equiv} \frac{\int_{\mathcal{F}_\psi \backslash 0} S[k\hat{\boldsymbol{e}}(\theta+\vartheta, \phi+\varphi) - k\hat{\boldsymbol{e}}(\theta,\phi)]d\vartheta\, d\varphi}{\oint_{\mathcal{S}\backslash 0} S[k\hat{\boldsymbol{e}}(\theta+\vartheta, \phi+\varphi) - k\hat{\boldsymbol{e}}(\theta,\phi)]d\vartheta\, d\varphi},$$
(G1)

$$T_\psi(\boldsymbol{k}_{\mathrm{inc}}) \underset{2d}{\equiv} \frac{\int_{\mathcal{F}_\psi \backslash 0} S[k\hat{\boldsymbol{e}}(\theta+\vartheta) - k\hat{\boldsymbol{e}}(\theta)]d\vartheta}{\oint_{\mathcal{C}\backslash 0} S[k\hat{\boldsymbol{e}}(\theta+\vartheta) - k\hat{\boldsymbol{e}}(\theta)]d\vartheta},$$
(G2)

where $\mathcal{F}_\psi$ is a forward cone with half-aperture angle ψ. In the limit $\psi = \pi/2$, in both $2d$ and $3d$, the cone becomes a half circle or sphere, and the previous definition is recovered.

We sketch the effect of the aperture ψ in Fig. 12(a): As the aperture angle is reduced from $\pi/2$, the smallest frequency at which forward scattering reaches the detector is pushed to higher and higher frequencies. More precisely, the onset is expected at $k_f(\psi) = K/\sqrt{2(1-\cos\psi)}$, so that $k_f(\pi/2) = K/\sqrt{2}$ as in the main text, and $k_f(0) \to \infty$, so that the width of the observed trough is unbounded from above. To illustrate this, we show intensity maps for this quantity, for a few values of ψ, in Figs. 12(b)–12(d), in a stealthy hyperuniform system of $N = 4 \times 10^7$ particles with $K = 3000$. We indeed observe that switching from $\psi = \pi/2$ to $\psi = \pi/4$ leads to a roughly twofold change in the value of k_f, leading to a large change in the perceived width of the transmission trough.

APPENDIX H: SATURATING PEAKS AND ECHOES IN NUwNU CONSTRAINTS

Here we show that constraining a set of N_k peaks to their maximum real value, $S(\boldsymbol{k}_j) = N$, $j = 1, \ldots, N_k$, also implicitly constrains peaks at all integer linear combinations of the $\boldsymbol{k}_j$ at which the original constraints are imposed. This can be shown analytically: Starting from the expression for the structure factor of a point pattern with positions $\boldsymbol{r}_n$, $n = 1, \ldots, N$

at the specified coordinates $\boldsymbol{k}_j$,

$$S(\boldsymbol{k}_j) \equiv \frac{|\widehat{\rho}(\boldsymbol{k}_j)|^2}{N} = N,$$
(H1)

where

$$\widehat{\rho}(\boldsymbol{k}_j) \equiv \sum_{n=1}^N \exp(i\boldsymbol{k}_j \cdot \boldsymbol{r}_n).$$
(H2)

Viewing the definition of $\widehat{\rho}(\boldsymbol{k}_j)$ as a sum of N unit length vectors in the complex plane, it can be concluded that in order to get $|\widehat{\rho}(\boldsymbol{k}_j)| = N$, all such unit-length vectors must point in the same direction. This means that, given one of the N_k vectors $\boldsymbol{k}_j$ at which the constraint is imposed, all N dot products $\boldsymbol{k}_j \cdot \boldsymbol{r}_n = \zeta + 2\pi m$ with $\zeta \in [-\pi;\pi)$ a constant and $m \in \mathbb{Z}$, meaning that the dot products all represent the same phase angle (accounting for shifts of integer multiples of 2π). In real space, this means that the projections of the points positions onto the direction of $\boldsymbol{k}$ are a subset of sites on a periodic $1d$ lattice with period $\lambda = 2\pi/|\boldsymbol{k}|$. However, this does not guarantee generically that all $\boldsymbol{k}_j \cdot \boldsymbol{r}$ are the same, i.e., it is possible that $\boldsymbol{k}_j \cdot \boldsymbol{r}_n \neq \boldsymbol{k}_{l\neq j} \cdot \boldsymbol{r}_n$ (they can project to different sites of the $1d$ lattice).

Given the above constraint, the structure factor at a k-space coordinate $\boldsymbol{s} = \sum_j C_j \boldsymbol{k}_j$, with $C_j \in \mathbb{Z}$ an arbitrary linear combination of the constrained $\boldsymbol{k}_j$, reads

$$\widehat{\rho}(\boldsymbol{s}) = \sum_{n=1}^N \exp(i\boldsymbol{s} \cdot \boldsymbol{r}) \equiv \sum_{n=1}^N \exp\left(i\sum_j C_j \boldsymbol{k}_j \cdot \boldsymbol{r}_n\right). \quad (\text{H3})$$

For any two generic points $\boldsymbol{r}_n$ and $\boldsymbol{r}_m$ and one specific $\boldsymbol{k}_j$, we showed that $\boldsymbol{k}_j \cdot \boldsymbol{r}_n = \boldsymbol{k}_j \cdot \boldsymbol{r}_m + 2\pi c$ for some $c \in \mathbb{Z}$. We then have

$$\begin{aligned}
\exp(iC_j\boldsymbol{k}_j \cdot \boldsymbol{r}_n) &= \exp(iC_j(\boldsymbol{k}_j \cdot \boldsymbol{r}_m + 2\pi c)) \\
&= \exp(iC_j\boldsymbol{k}_j \cdot \boldsymbol{r}_m)\exp(i2\pi cC_j) \\
&= \exp(iC_j\boldsymbol{k}_j \cdot \boldsymbol{r}_m),
\end{aligned}$$
(H4)

as $cC_j \in \mathbb{Z}$. All terms in Eq. (H3) are thus equal, so that we may write $\widehat{\rho}(\boldsymbol{s})$ in terms of only one point coordinate $\boldsymbol{r}_1$ then
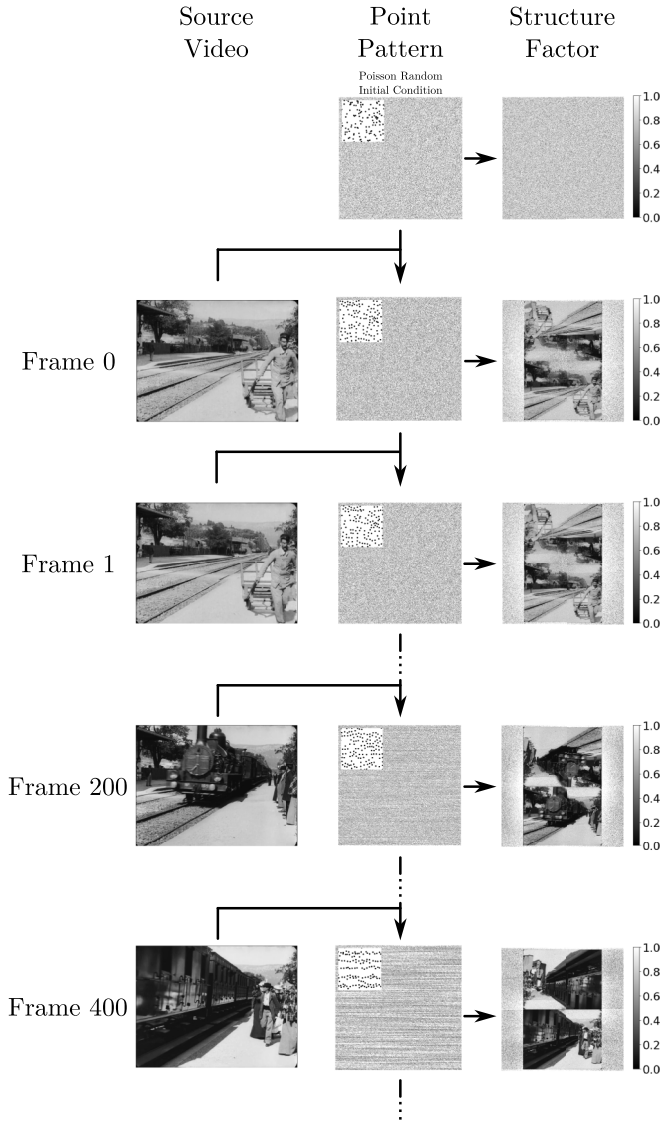
FIG. 13. Construction and example frames of spectral movie. Left: Frames from source video *L'Arrivée d'un Train en Gare de La Ciotat* [52]. Middle: Minimized point patterns ($N = 300\,000$) from imposing the source video frame as a constraint in $S(k)$, with an inset showing a zoomed-in region of the point pattern. Right: The calculated structure factor of the resulting minimized point pattern. The video is also available.

use the definition of s,

$$\widehat{\rho}(s) = N \prod_j \exp(iC_j \mathbf{k}_j \cdot \mathbf{r}_1) = N \exp(i\mathbf{s} \cdot \mathbf{r}_1), \qquad \text{(H5)}$$

so that, finally,

$$S(\mathbf{s}) = N. \qquad \text{(H6)}$$

In other words, we have shown that any set of N-high peaks imposed into the structure factor has N-high echoes, located at all integer linear combinations of the imposed peaks.

Due to the limitations of dimensionality, one cannot enforce arbitrarily many peaks of intensity N in S. In fact, the greatest number of peaks one can arbitrarily impose that will reach an exact value of $S(\mathbf{k}) = N$ is d, the number of dimensions, resulting in only the primitive Bravais lattices (generically monoclinic in $2d$ and triclinic in $3d$). With our algorithm, overconstrained cases such as crystals with motifs of more than one atom or quasicrystals seek to maximize the value of all peaks. Thus, we still observe quasicrystalline structures emerge from our NUwNU protocol.

APPENDIX I: ENCODING MOVIES INTO SUCCESSIVE $S(k)$

As we have demonstrated the ability to encode images into the structure factor of point patterns, here we encode a movie by an iterative minimization process (Fig. 13). We impose each frame extracted from the movie *L'Arrivée d'un train en gare de La Ciotat* ("The Arrival of a Train at La Ciotat Station") [52] (962×720 px) as constraints $S_0(\mathbf{k})$ on systems of $N = 300\,000$ points in $2d$. The full 810 frame video depicting the simultaneous evolution of the point pattern and its measured structure factor is available as video in SM [35]. The point pattern based on frame 0 was minimized from a Poisson random initial condition, while all subsequent points patterns are minimized using the point pattern encoding the previous frame as an initial condition. By performing this successive minimization, we can encode the movie into discrete point trajectories. Due to the similarity between successive frames in a single-take sequence shot, successive minimizations are faster than minimizations from random configurations and point trajectories themselves are seemingly close to continuous. This opens up the possibility of smoothly evolving adaptive point patterns with spectrally shaped disorder.

[1] C. Kittel, *Introduction to Solid-State Physics* (John Wiley & Sons, New York, 1953).

[2] R. Carminati and J. C. Schotland, *Principles of Scattering and Transport of Light* (Cambridge University Press, Cambridge, UK, 2021).

[3] K. Vynck, R. Pierrat, R. Carminati, L. S. Froufe-Pérez, F. Scheffold, R. Sapienza, S. Vignolini, and J. J. Sáenz, Light in correlated disordered media, Rev. Mod. Phys. **95**, 045003 (2023).

[4] K. Djeghdi, U. Steiner, and B. D. Wilts, 3D tomographic analysis of the order-disorder interplay in the *Pachyrhynchus congestus mirabilis* weevil, Adv. Sci. **9**, 2202145 (2022).

[5] K. Vynck, R. Pacanowski, A. Agreda, A. Dufay, X. Granier, and P. Lalanne, The visual appearances of disordered optical metasurfaces, Nat. Mater. **21**, 1035 (2022).

[6] M. Florescu, S. Torquato, and P. J. Steinhardt, Designer disordered materials with large, complete photonic band gaps, Proc. Natl. Acad. Sci. USA **106**, 20658 (2009).

[7] W. Man, M. Florescu, K. Matsuyama, P. Yadak, G. Nahal, S. Hashemizad, E. Williamson, P. Steinhardt, S. Torquato, and P. Chaikin, Photonic band gap in isotropic hyperuniform disordered solids with low dielectric contrast, Opt. Express **21**, 19972 (2013).

[8] L. S. Froufe-Pérez, M. Engel, J. J. Sáenz, and F. Scheffold, Band gap formation and Anderson localization in disordered photonic materials with structural correlations, Proc. Natl. Acad. Sci. USA **114**, 9570 (2017).

[9] R. Monsarrat, R. Pierrat, A. Tourin, and A. Goetschy, Pseudo-gap and Anderson localization of light in correlated disordered media, Phys. Rev. Res. **4**, 033246 (2022).

[10] D. M. Yan, J. W. Guo, B. Wang, X. P. Zhang, and P. Wonka, A survey of blue-noise sampling and its applications, J. Comput. Sci. Technol. **30**, 439 (2015).

[11] M. Pharr, W. Jakob, and G. Humphreys, *Physically Based Rendering: From Theory to Implementation*, 3rd ed. (Morgan Kaufmann, Burlington, MA, 2018).

[12] A. Pilleboue, G. Singh, D. Coeurjolly, M. Kazhdan, and V. Ostromoukhov, Variance analysis for Monte Carlo integration, ACM Trans. Graph. **34**, 1 (2015).

[13] S. Torquato, Hyperuniform states of matter, Phys. Rep. **745**, 1 (2018).

[14] M. A. Klatt, P. J. Steinhardt, and S. Torquato, Wave propagation and band tails of two-dimensional disordered systems in the thermodynamic limit, Proc. Natl. Acad. Sci. USA **119**, e2213633119 (2022).

[15] J. Haberko, L. S. Froufe-Pérez, and F. Scheffold, Transition from light diffusion to localization in three-dimensional amorphous dielectric networks near the band edge, Nat. Commun. **11**, 4867 (2020).

[16] O. U. Uche, F. H. Stillinger, and S. Torquato, Constraints on collective density variables: Two dimensions, Phys. Rev. E **70**, 046122 (2004).

[17] O. U. Uche, S. Torquato, and F. H. Stillinger, Collective coordinate control of density distributions, Phys. Rev. E **74**, 031104 (2006).

[18] P. K. Morse, J. Kim, P. J. Steinhardt, and S. Torquato, Generating large disordered stealthy hyperuniform systems with ultra-high accuracy to determine their physical properties, Phys. Rev. Res. **5**, 033190 (2023).

[19] L. S. Froufe-Pérez, M. Engel, P. F. Damasceno, N. Muller, J. Haberko, S. C. Glotzer, and F. Scheffold, Role of short-range order and hyperuniformity in the formation of band gaps in disordered photonic materials, Phys. Rev. Lett. **117**, 053902 (2016).

[20] O. Leseur, R. Pierrat, and R. Carminati, High-density hyperuniform materials can be transparent, Optica **3**, 763 (2016).

[21] S. Gorsky, W. A. Britton, Y. Chen, J. Montaner, A. Lenef, M. Raukas, and L. D. Negro, Engineered hyperuniformity for directional light extraction, APL Photon. **4**, 110801 (2019).

[22] S. Torquato and J. Kim, Nonlocal effective electromagnetic wave characteristics of composite media: Beyond the quasistatic regime, Phys. Rev. X **11**, 021002 (2021).

[23] V. van Gogh, The Starry Night (1889) Museum of Modern Art (New York), Oil-on-canvas painting.

[24] Y. Jiao and S. Torquato, Maximally random jammed packings of Platonic solids: Hyperuniform long-range correlations and isostaticity, Phys. Rev. E **84**, 041309 (2011).

[25] L. Corté, P. M. Chaikin, J. P. Gollub, and D. J. Pine, Random organization in periodically driven systems, Nat. Phys. **4**, 420 (2008).

[26] D. Hexner and D. Levine, Hyperuniformity of critical absorbing states, Phys. Rev. Lett. **114**, 110602 (2015).

[27] D. Levine and P. J. Steinhardt, Quasicrystals: A new class of ordered structures, Phys. Rev. Lett. **53**, 2477 (1984).

[28] J.-P. Hansen and I. R. McDonald, *Theory of Simple Liquids* (Elsevier Academic Press, San Diego, CA, 2006).

[29] D. Schwarzenbach, *Crystallography* (John Wiley & Sons, New York, 1996).

[30] A. H. Barnett, J. Magland, and L. Af Klinteberg, A Parallel nonuniform fast Fourier transform library based on an "exponential of semicircle" kernel, SIAM J. Sci. Comput. **41**, C479 (2019).

[31] A. H. Barnett, Aliasing error of the $\exp(\beta\sqrt{1-z^2})$ kernel in the nonuniform fast fourier transform, Appl. Comput. Harmon. Anal. **51**, 1 (2021).

[32] D. C. Liu and J. Nocedal, On the limited memory BFGS method for large-scale optimization, Math. Program. **45**, 503 (1989).

[33] J. Nocedal and S. Wright, *Numerical Optimization* (Springer, Berlin, 1999).

[34] https://github.com/martiniani-lab/FReSCo.

[35] See Supplemental Material at http://link.aps.org/supplemental/10.1103/PhysRevE.110.034122 for a full derivation of the Ewald construction and a comparison to a direct measurement of single-scattering properties, as well as additional data. The additional data include bond-orientational order parameter distributions and pair correlation functions in quasicrystalline systems, extra projections of the 3*d* icosahedral and dodecahedral systems, and an example video of point trajectories that encode a target movie in their structure factor, and which includes Refs. [58–67].

[36] S. F. Liew, J. K. Yang, H. Noh, C. F. Schreck, E. R. Dufresne, C. S. O'Hern, and H. Cao, Photonic band gaps in three-dimensional network structures withshort-range order, Phys. Rev. A **84**, 063818 (2011).

[37] N. Muller, J. Haberko, C. Marichy, and F. Scheffold, Silicon hyperuniform disordered photonic materials with a pronounced gap in the shortwave infrared, Adv. Opt. Mater. **2**, 115 (2014).

[38] J. Kim and S. Torquato, Multifunctional composites for elastic and electromagnetic wave propagation, Proc. Natl. Acad. Sci. USA **117**, 8764 (2020).

[39] A. Vrij, Light scattering of a concentrated multicomponent system of hard spheres in the Percus-Yevick approximation, J. Chem. Phys. **69**, 1742 (1978).

[40] Y. Rosenfeld, Free-energy model for the inhomogeneous hard-sphere fluid in *D* dimensions: Structure factors for the hard-disk (*D*=2) mixtures in simple explicit form, Phys. Rev. A **42**, 5978 (1990).

[41] E. P. Bernard, W. Krauth, and D. B. Wilson, Event-chain Monte Carlo algorithms for hard-sphere systems, Phys. Rev. E **80**, 056704 (2009).

[42] J. Bertolotti, E. G. V. Putten, C. Blum, A. Lagendijk, W. L. Vos, and A. P. Mosk, Non-invasive imaging through opaque scattering layers, Nature (Lond.) **491**, 232 (2012).

[43] A. Lagae, S. Lefebvre, R. Cook, T. DeRose, G. Drettakis, D. S. Ebert, J. P. Lewis, K. Perlin, and M. Zwicker, A survey of procedural noise functions, Comput. Graph. Forum **29**, 2579 (2010).

[44] Z. Ma and S. Torquato, Random scalar fields and hyperuniformity, J. Appl. Phys. **121**, 244904 (2017).

[45] M. Engel, P. F. Damasceno, C. L. Phillips, and S. C. Glotzer, Computational self-assembly of a one-component icosahedral quasicrystal, Nat. Mater. **14**, 109 (2015).

[46] F. Sgrignuoli and L. D. Negro, Hyperuniformity and wave localization in pinwheel scattering arrays, Phys. Rev. B **103**, 224202 (2021).

[47] L.-Y. Wei, Multi-class blue noise sampling, ACM Trans. Graph. **29**, 79 (2010).

[48] F. de Goes, K. Breeden, V. Ostromoukhov, and M. Desbrun, Blue noise through optimal transport, ACM Trans. Graph. **31**, 1 (2012).

[49] D. Heck, T. Schlomer, and O. Deussen, Blue noise sampling with controlled aliasing, ACM Trans. Graph. **32**, 1 (2013).

[50] E. Heitz, L. Belcour, V. Ostromoukhov, D. Coeurjolly, and J. C. Iehl, A low-discrepancy sampler that distributes Monte Carlo errors as a blue noise in screen space, in ACM SIGGRAPH 2019 Talks (ACM, New York, 2019).

[51] A. Wolfe, N. Morrical, T. Akenine-Moller, and R. Ramamoorthi, Spatiotemporal blue noise masks, in *Eurographics Symposium on Rendering* (The Eurographics Association, 2021), pp. 117–126.

[52] A. Lumière and L. Lumière, Arrivée d'un Train en Gare de La Ciotat, Société Lumière (1896).

[53] R. L. McGreevy, Reverse Monte Carlo modelling, J. Phys.: Condens. Matter **13**, R877 (2001).

[54] F. H. Stillinger and T. A. Weber, Computer simulation of local order in condensed phases of silicon, Phys. Rev. B **31**, 5262 (1985).

[55] J. Sunseri, Z. Slepian, S. Portillo, J. Hou, S. Kahraman, and D. P. Finkbeiner, Sarabande : 3/4 point correlation functions with fast Fourier transforms, RAS Tech. Instrum. **2**, 62 (2023).

[56] C. P. Goodrich, E. M. King, S. S. Schoenholz, E. D. Cubuk, and M. P. Brenner, Designing self-assembling kinetics with differentiable statistical physics models, Proc. Natl. Acad. Sci. USA **118**, e2024083118 (2021).

[57] E. van der Velden, CMasher: Scientific colormaps for making accessible, informative and 'cmashing' plots, J. Open Source Softw. **5**, 2004 (2020).

[58] M. Morse, Philip, and H. Feshbach, *Methods of Theoretical Physics: Part I* (McGraw–Hill, New York, 1953).

[59] E. N. Economou, *Springer Series in Solid-state Sciences* (Springer, Berlin, 2006).

[60] Á. González, Measurement of areas on a sphere using Fibonacci and latitude-longitude lattices, Math. Geosci. **42**, 49 (2010).

[61] V. H. Lutfalla, An effective construction for cut-and-project rhombus tilings with global n-fold rotational symmetry, in *Proceedings of the 27th IFIP WG 1.5 International Workshop on Cellular Automata and Discrete Complex Systems (AUTOMATA'21)*, edited by A. Castillo-Ramirez, P. Guillon, and K. Perrot (Dagstuhl, Germany, 2021), pp. 9:1–9:12.

[62] N. G. de Bruijn, Algebraic theory of Penrose's non-periodic tilings of the plane. I, Indagationes Math. (Proc.) **84**, 39 (1981).

[63] N. de Bruijn, Quasicrystals and their Fourier transform, Indagat. Math. (Proc.) **89**, 123 (1986).

[64] D. Levine and P. J. Steinhardt, Quasicrystals. I. Definition and structure, Phys. Rev. B **34**, 596 (1986).

[65] P. J. Steinhardt, D. R. Nelson, and M. Ronchetti, Bond-orientational order in liquids and glasses, Phys. Rev. B **28**, 784 (1983).

[66] D. R. Nelson and B. I. Halperin, Dislocation-mediated melting in two dimensions, Phys. Rev. B **19**, 2457 (1979).

[67] Y.-W. Li and M. P. Ciamarra, Attraction tames two-dimensional melting: From continuous to discontinuous transitions, Phys. Rev. Lett. **124**, 218002 (2020).

[68] S. Torquato, G. Zhang, and F. H. Stillinger, Ensemble theory for stealthy hyperuniform disordered ground states, Phys. Rev. X **5**, 021020 (2015).

[69] J. R. Fienup, Phase retrieval algorithms: A comparison, Appl. Opt. **21**, 2758 (1982).

[70] J. Dong, J. Liu, K. Yao, M. Chantler, L. Qi, H. Yu, and M. Jian, Survey of procedural methods for two-dimensional texture generation, Sensors **20**, 1135 (2020).

[71] A. Gabrielli and S. Torquato, Voronoi and void statistics for superhomogeneous point processes, Phys. Rev. E **70**, 041105 (2004).